Pergamon

Acta mater. Vol. 46, No. 11, pp. 4037–4065, 1998
© 1998 Acta Metallurgica Inc.
Published by Elsevier Science Ltd. All rights reserved
Printed in Great Britain
PII: S1359-6454(98)00040-8
1359-6454/98 $19.00 + 0.00

HIGH-STRAIN-RATE DEFORMATION OF GRANULAR SILICON CARBIDE

C. J. SHIH[1,2], M. A. MEYERS[1,2]† and V. F. NESTERENKO[2]

[1]Institute for Mechanics and Materials, [2]Department of Applied Mechanics and Engineering Sciences, University of California, San Diego, La Jolla, CA 92093, U.S.A.

(Received 12 August 1997; accepted 23 January 1998)

Abstract—Silicon carbide powders with three particle size distributions (average sizes of 0.4, 3 and 50 μm) were subjected to strain-controlled, high-strain-rate deformation ($\dot{\varepsilon}\approx 3\times 10^4$/s) in a cylindrical geometry which imposed simultaneous compressive stresses. The experiments involved two explosive stages to (a) densify the powder and to (b) subject the densified granules to large deformation. The powder, with initial density of 33–59% of theoretical density, was densified to densities between 73 and 94% of theoretical density in the first stage. The densified powders were subjected to a global effective strain of ≈ -0.27 in the second stage. Their response to the imposed constraints occurred through both homogeneous deformation (82–100%) and shear localization (0–18%), depending on the particle size. In the coarse powder (50 μm), the shear localization process was primarily due to particle break-up (comminution) and rearrangement of the comminuted particles, through a similar mechanism to the bulk and prefractured SiC (Shih, C. J., Nesterenko, V. F. and Meyers, M. A., *Journal of Applied Physics*, 1998, **83**, 4660). Comminution was observed in the medium powder (3 μm), but was never seen in the fine powder (0.4 μm). In medium and fine granular SiC, the shear localization at sufficiently high displacement (>150 μm) leads to the formation of a thin layer (5–20 μm) of well-bonded material. Calculated temperatures in the centers of the bands are up to 2300°C (using an assumed shear strength of 2 GPa and linear thermal softening), which explain the bonding. An analytical model is developed that correctly predicts break-up of large particles and plastic deformation of the smaller ones. It is based on the Griffith fracture criterion and Weibull distribution of strength, which quantitatively express the fact that the fracture is generated by flaws the size of which is limited by the particle size. © *1998 Acta Metallurgica Inc.*

1. INTRODUCTION

The development of heavy armor that can resist modern kinetic and chemical-energy penetrators has a high importance. Ceramics are a critical component in modern armor systems. The recovery experiments by Shockey *et al.* [1] show in a clear way the different regions of damage in ceramics subjected to high-velocity impact. Viechnicki *et al.* [2] and Meyers [3] classified the damage produced in a ceramic into

(i) a comminuted zone (also known as Mescall zone);
(ii) radial and conical cracks caused by radially expanding stress waves;
(iii) spalling generated by reflected, tensile pulses; and
(iv) damage due to the flow of the comminuted material.

The flow of this comminuted ceramic proceeds in a constrained volumetric condition because the surrounding material imposes a lateral confinement. Curran *et al.* [4] developed a micromechanical model for the flow of this comminuted (granular) material under high-strain-rate deformation. They consider sliding and ride-up of fragments, with competition between dilatation and pore compaction. They concluded that the inelastic deformation of the comminuted material plays a key role in the resistance of ceramic to penetration. For example, a threefold increase in the inter-particle friction decreases the penetration depth by a factor of three.

Hauver and coworkers [5–7] showed convincingly that the design of armor has a very significant effect on its efficiency. By introducing target modifications which minimize the damage, they were able to dramatically increase the penetration resistance of the ceramic. Hence, the decrease of internal damage and containment of the damaged ceramic are essential issues of armor design. The inelastic deformation of the damaged, granular ceramic is a key stage in the penetration of armor. Granular materials are known to undergo shear localization during quasistatic, inelastic deformation, in the presence of superimposed confinement stresses [8–21]. Klopp and Shockey [22] examined initially solid SiC at high strain rate, using symmetric pressure/shear plate-impact experiments. The results indicated that comminution occurs soon after loading. The strength of the highly comminuted material was found to increase monotonically with the con-

†To whom all correspondence should be addressed.

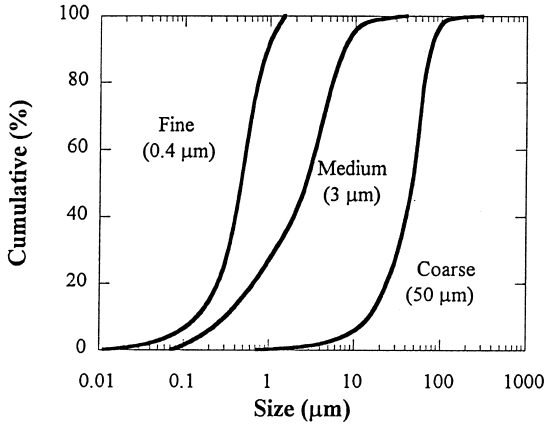

Fig. 1. Cumulative size distributions for three SiC powders.

fining pressure, and was about one sixth of the strength of uncomminuted material. The strength of comminuted material at high strain rate ($\approx 10^5$/s) was found to be significantly lower than the strength under quasistatic loading. However, it should be pointed out that there might be some problems in the interpretation of their results because of spallation under pure shear, as discussed by Espinosa and Clifton [23]. A newer method of pressure-shear loading using window interferometry, developed by Espinosa [24], overcomes the aforementioned limitation.

Recently, Nesterenko *et al.* [25] showed that densified granular Al_2O_3, subjected to strains between 0.2 and 0.4 at strain rate of 3×10^4/s in a cylindrical collapse geometry, exhibited profuse shear-band formation. Significant differences in the deformation mechanisms were observed in granular Al_2O_3 with two particle sizes: 0.4 and 4 μm. In comparison with quasistatic deformation of granular materials, the shear patterning under dynamic conditions is affected by particle fracture. The objective of this investigation was to extend the large strain, high-strain-rate study to silicon carbide (SiC), a very important ceramic for armor applications. This program consists of two parts: solid and granular SiC, and both materials are subjected to identical experimental conditions. In the first part [26], fully dense solid SiC was subjected to an explosive shock wave for fragmentation. The fragmented ceramic was then deformed in a collapsing cylinder geometry. Shear localization was the primary mode of deformation. The second part of this program is described in this paper; it focuses on granular SiC. In order to examine the effect of particle size and porosity, three size ranges were chosen for SiC powders: 0.4, 3 and 50 μm (mean values). The experiments are designed to examine the ceramic flow under superimposed confinement pressure, representing the behavior of the ceramic adjacent to the projectile.

2. EXPERIMENTAL PROCEDURES

Silicon carbide powders with three different particle sizes were used in this investigation. The fine powder was produced by H.C. Starck (Grade UF-15), the medium powder was fabricated by Nagasse (Grade GMF-6S), and coarse powder was manufactured by Norton (Grade F230). The average particle sizes for the small, medium and coarse powders were 0.4, 3 and 50 μm, respectively. As shown in Fig. 1, all powders have a wide range of particle size distribution; nevertheless, these three powders represent particle sizes of two order of magnitude of difference. These powders all have the α-SiC crystal structure, and "chunky" morphology, as shown in Fig. 2.

The thick-walled cylinder method was used to investigate the high-strain-rate deformation (3×10^4/s) of granular silicon carbide. Experiments were conducted on three fine, two medium, and three coarse powder specimens, which were tested under identical conditions. The experimental procedures were originally developed for metals and were later modified for granular and brittle materials [27–31]. The procedure consists of two explosive events: the first event to densify the ceramic and the second event to deform the densified ceramic.

The experimental procedures are outlined in Fig. 3, and are described in detail by Nesterenko *et al.* [25]. Silicon carbide powder was loaded into a tubular cavity made up by a central copper rod (14.5 mm diameter) and an outer copper tube (24.6 mm inner diameter and 38 mm outer diameter). A mixture of 3:1 volume ratio of ammonite and sand was used to generate an explosion of low detonation velocity (3.2 km/s) to densify the SiC cylinder. A cylindrical orifice (11 mm diameter) was then drilled in the center of the copper insert. The specimen then underwent another explosive event using 100% ammonite to achieve a detonation velocity of 4.2–4.4 km/s to collapse the center orifice. This explosive event produced large inelastic deformation and profuse shear bands; the shear-band displacement is marked as Δ in Fig. 3(c).

The global strains can be obtained from the strains in the incompressible copper, i.e. the cross-sectional area of copper along the longitudinal axis remains the same during deformation [28]. The radial and tangential engineering strains (e_{rr} and $e_{\varphi\varphi}$) and effective strain (ε_{eff}) can be estimated from the initial and final radii, r_o and r_f [Fig. 3(d)]:

$$e_{rr} = \frac{r_o}{r_f} - 1$$

$$e_{\varphi\varphi} = \frac{r_f}{r_o} - 1$$

$$\varepsilon_{eff} = \frac{2}{\sqrt{3}} \ln\left(\frac{r_o}{r_f}\right) \quad (1)$$

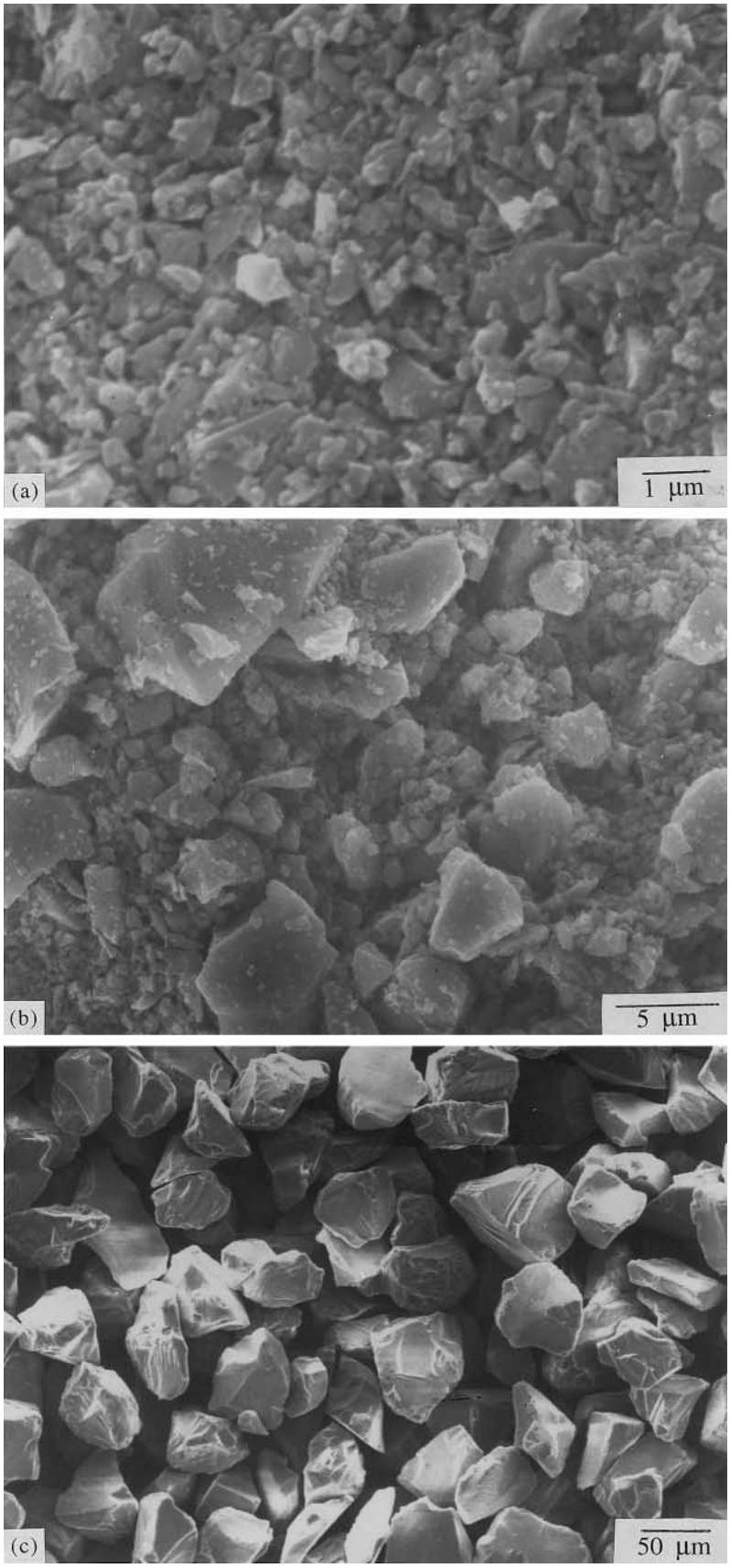

Fig. 2. SiC powders used in the experiments: (a) fine powder (0.4 μm); (b) medium powder (3 μm); (c) coarse powder (50 μm).

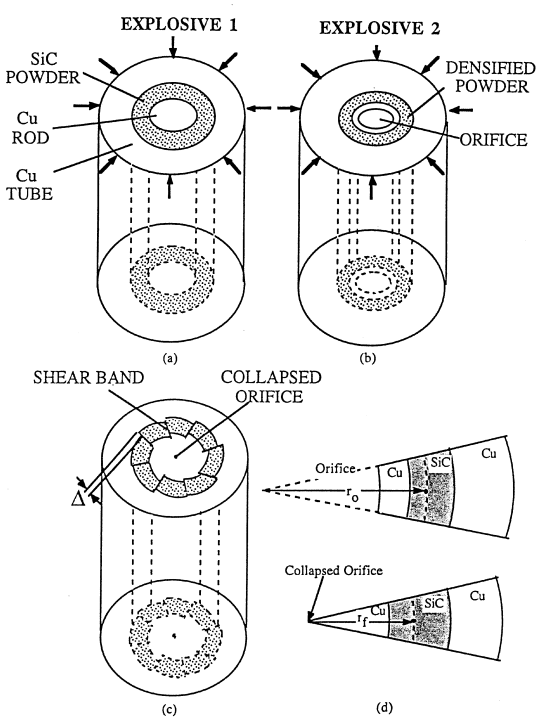

Fig. 3. Experimental steps for densification and deformation of granular SiC. (a) Explosive event 1: densification; (b) explosive 2: deformation; (c) final configuration; (d) initial and final radii during deformation.

The global tangential strains ($e_{\varphi\varphi}$) were −0.35 and −0.10 along the inner and outer radii, respectively. The strain rate during the test is calculated from the measured displacement of the inner wall of the cylinder during the collapse process [28], and the strain rate is approximately 3×10^4/s.

After collapse, the thick-walled composite cylinders were sectioned with a diamond saw and polished by diamond paste. The sections were inserted in a vacuum desiccator and impregnated with epoxy to increase the resistance of the granules and fragments to pull-out. As-received powders were also subjected to the same sectioning and polishing process and results indicated that the specimen preparation process did not contribute to the particle fracturing observed after explosive specific loading.

3. RESULTS AND DISCUSSION

Three fine, two medium and three coarse powder specimens were tested under identical conditions. The compact density (after powder was loaded into the cavity), densified density (after the first explosive event) and deformed density (after the second explosive event) are listed in Table 1. The density of a powder compact is determined by the particle characteristics, such as size distribution and morphology. As shown in Table 1, the initial powder packing density varied from 33 to 56% of the theoretical density. After the first explosive event, approximately 83–88% of theoretical density was achieved. The second explosive event reduced the density to about 63–78% of the theoretical density.

3.1. Densification in the first explosive event

The objective of the first explosive event was to densify the powder compact through compressive loading. SEM analysis indicated that the microstructure was uniform from the inner radius area to the outer radius region. As shown in Fig. 4, all densified ceramics had a bimodal particle distribution, consisting of large particles surrounded by small particles. Particle break-up can be clearly identified in the coarse and medium powder specimens. All powders had a wide range of particle size distribution, and the densification is mainly through (i) break-up of large particles and (ii) rearrangement of the comminuted particles to achieve a high packing density. These three different SiC powders represent particle sizes of two orders of magnitude difference. The largest particles in the fine powder are around 2 μm, and are much smaller than the smallest particles in the coarse powder.

3.2. Macroscopic deformation in the second explosive event

The overall view of samples with three ceramic particle sizes is shown in Fig. 5. Profuse shear local-

Table 1. Density of granular SiC after different stages

Powder type Average particle size	Specific number	Fine 0.4 μm	Medium 3 μm	Coarse 50 μm
Compact density	1	39%	34%	59%
	2	37%	33%	54%
	3	38%		56%
	Average	38 ± 1%	33 ± 1%	56 ± 2%
Densified density after the first explosive	1	73%	81%	92%
	2	87%	94%	84%
	3	88%		88%
	Average	83 ± 6%	87 ± 6%	88 ± 3%
Deformed density after the second explosive	1	67%	63%	78%
	2	77%	63%	78%
	3	66%		78%
	Average	70 ± 4%	63 ± 1%	78 ± 1%

ization can be seen for all of them. In the inner radius region, all shear bands followed roughly an angle of 45° with the radial direction, corresponding to the maximum shear direction. As shown in Fig. 5(d), the angle (θ) of the shear bands with respect to the radial direction increases as the trajectory moves towards the outer radius regions. The angle is determined by the magnitudes of the principal stresses and shear strength, and can be predicted from the Mohr–Coulomb flow criterion. However, the thick-walled cylinder experiments are strain controlled. The magnitude of the principal

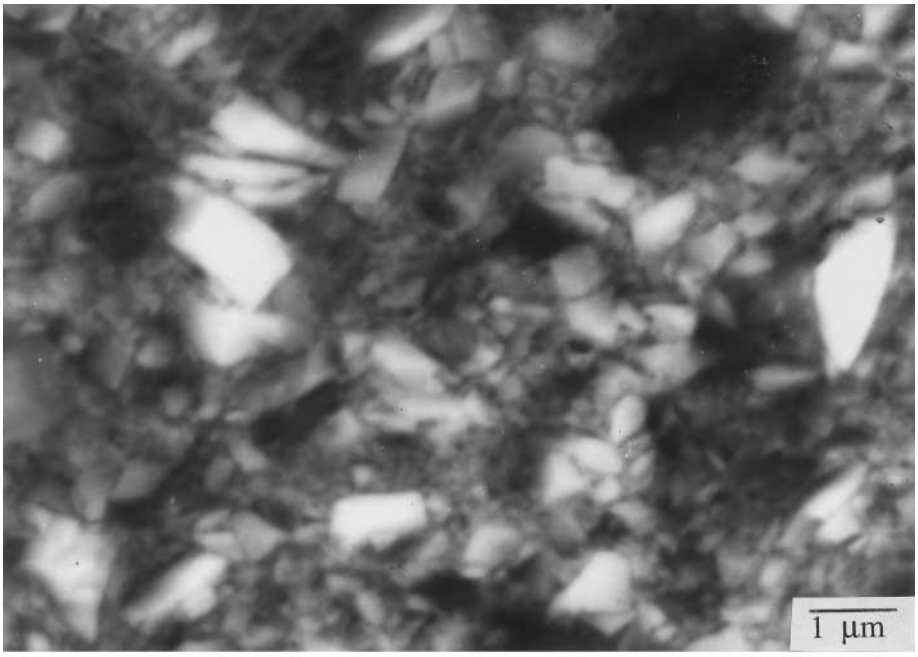

(a)

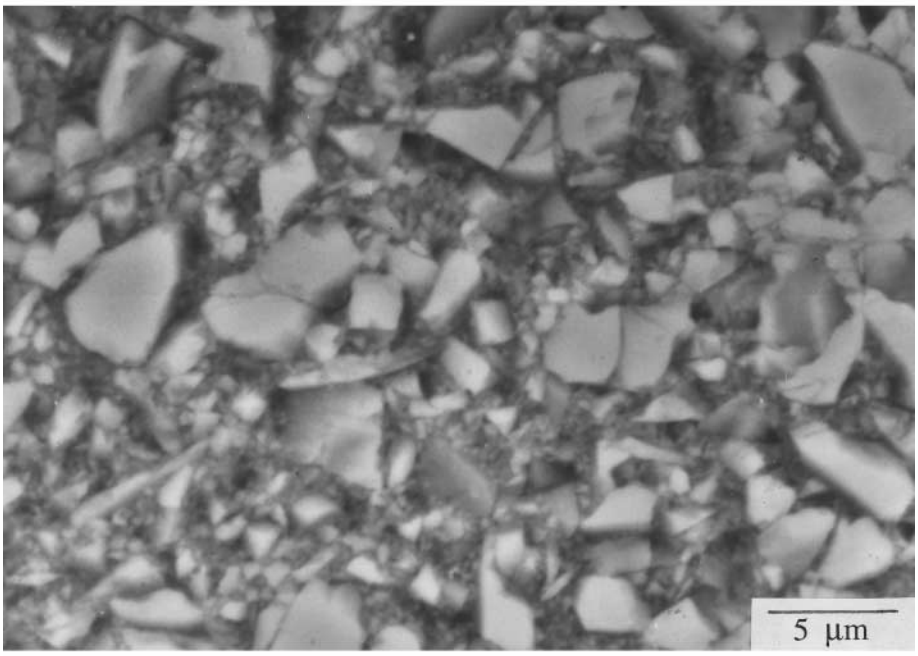

(b)

Fig. 4(a, b) (*caption overleaf*).

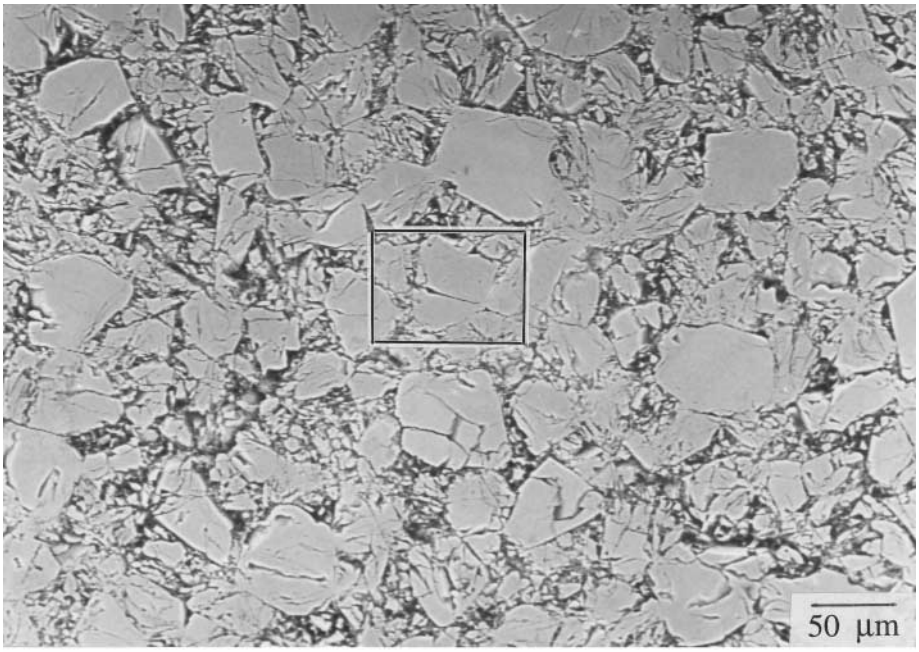

(c)

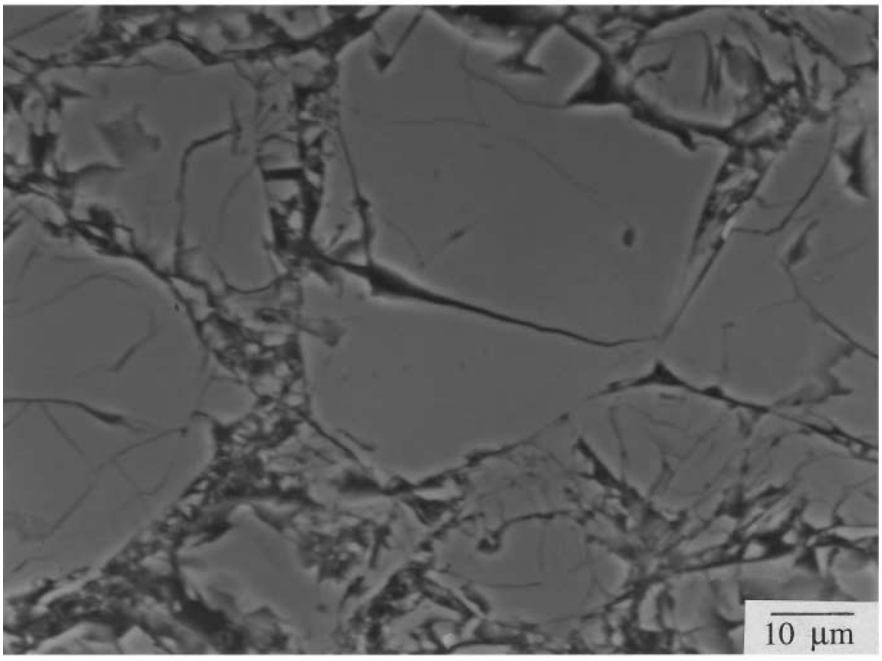

(d)

Fig. 4. Microstructure of densified SiC after the first explosive event: (a) fine powder; (b) medium powder; (c) coarse powder; (d) high magnification of coarse powder, showing cracking inside large particles.

stresses is not known, and the angle cannot be readily calculated. It is expected that the variation in angle is associated with the change in principal stresses from the inner radius to the outer radius. Nevertheless, the angle (θ) could provide a means to determine the resistance to flow.

The shear-band configurations for these eight granular specimens are summarized in Table 2.

Table 3 provides the shear-band configurations for prefractured SiC [26] for comparison purposes. The spacing between the shear bands is fairly regular, and varies from 0.4 to 1.2 mm. The shear-band spacing is significantly lower than the one for the prefractured SiC, described by Shih *et al.* [26]: the spacings vary between 1.7 and 3.1 mm. The same differences were observed between granular and prefractured Al_2O_3 [25, 30]. The average shear-band spacing for the prefractured Al_2O_3 is 2.0 mm, and the spacings are 0.49 and 0.61 mm for the granular Al_2O_3 with 0.4 and 4 μm particle size, respectively. In addition, the shear-band thickness also follows a similar trend. The average shear band thickness for the prefractured SiC is about 150 μm [26]; the shear band thicknesses are 40, 25 and 15 μm, for the granular SiC with 50, 3 and 0.4 μm particle size, respectively. These results show that the shear-band thickness is dependent on the type and condition of material: prefractured SiC has a much larger shear-band thickness

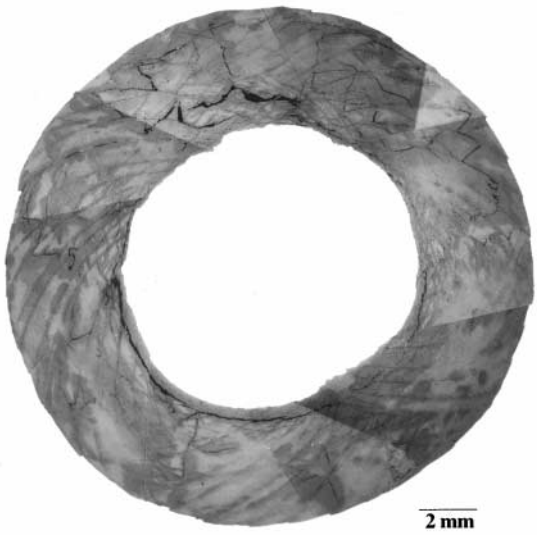

(a)

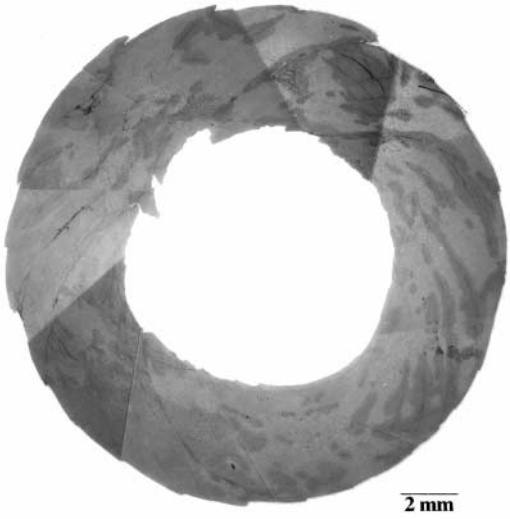

(b)

Fig. 5(a, b) (*caption overleaf*).

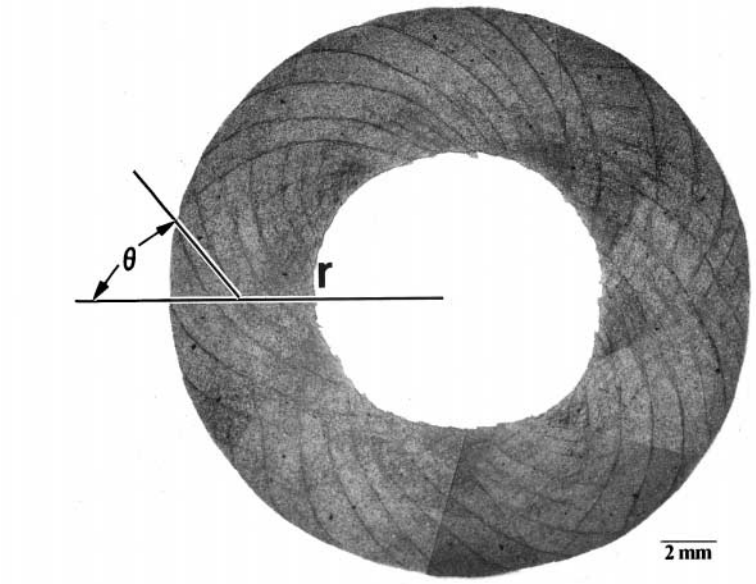

(c)

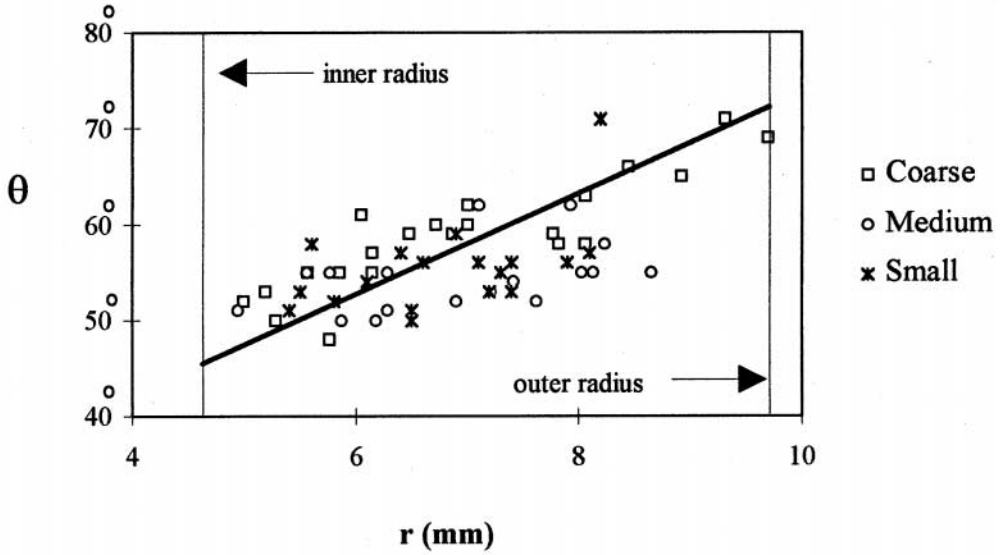

(d)

Fig. 5. Overall configuration after densification and deformation: (a) fine powder; (b) medium powder; (c) coarse powder; (d) relationship between the tangential angle and radius.

than the granular SiC. However, two order magnitude difference in the particle size in the granular SiC does not result in a proportional change of shear band thickness.

Grady and Kipp [32] proposed an analytical model to predict the fragment size ($\overline{L}$), based on the assumption that the kinetic and strain energies of the material prior to fragmentation is equal to the energy required to produce the cracks. The analysis relates the fragment size with the material resistance to crack propagation (toughness K_c), density (ρ), sonic velocity (C) and strain rate ($\dot{\varepsilon}$):

$$\overline{L} = \left(\frac{\sqrt{24} K_c}{\rho C \dot{\varepsilon}} \right)^{\frac{2}{3}}. \tag{2}$$

Table 2. Summary of shear-band configurations for granular SiC in different experiments

Particle size	0.4 μm	3 μm	50 μm
	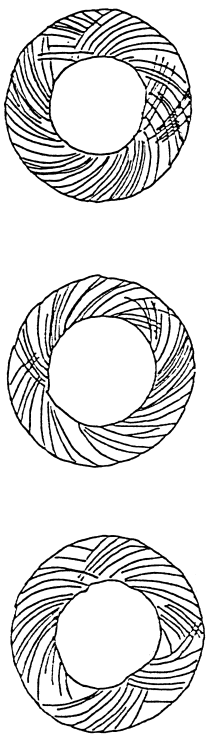	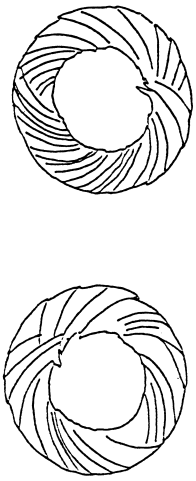	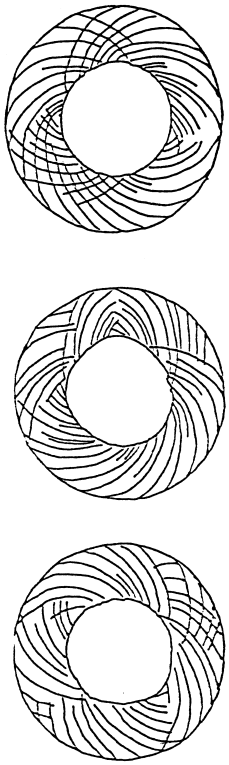
Number of groups	4 2 4	2 2	4 4 4
Number of shear bands	72 51 52	34 24	52 54 48
Average shear-band spacing	0.415 mm 0.583 mm 0.577 mm (0.525 $\pm$ 0.073 mm)	0.863 mm 1.202 mm (1.033 $\pm$ 0.170 mm)	0.624 mm 0.572 mm 0.660 mm (0.619 $\pm$ 0.031 mm)
Average displacement Δ	26 μm 41 μm 37 μm (35 $\pm$ 6 μm)	72 μm 133 μm (102 $\pm$ 30 μm)	0 μm 0 μm 0 μm (0 $\pm$ 0 μm)

This equation for fragment size can be extended to shear-band spacing and thickness. It provides important qualitative trends, such as the effects of strain rate and the resistance to shear. Granular materials have a lower resistance to shear flow than prefractured bulk materials, and have a lower shear-band spacing and thickness, in agreement with equation (2).

Both clockwise and counterclockwise shear bands can be identified. As shown in Table 2, there were either two or four groups of the clockwise and counterclockwise shear bands. This grouping is indicative of cooperative material motion and self-organization among the bands.

The partitioning of global strain (e_t) into homogeneous deformation (e_h) and deformation localized in shear bands (e_s) was carried out in a manner identical to the one described by Shih *et al.* [26]:

$$e_t = e_s + e_h. \tag{3}$$

The strains during the second explosive events are listed in Table 4. The global tangential strains (e_t) for these three SiC powders were almost identical (–0.21). However, the shear-band strain (e_s) varied from 0 to –0.038. The coarse powders did not exhibit any distinguishable shear displacement, although their shear bands can be clearly identified. The medium-sized powders had the highest amount of deformation localized in shear bands.

3.2.1. Deformation of coarse granular SiC. Even though shear bands were clearly identified in the coarse granular SiC, the shear-band displacement (Δ) is negligible, as shown in Fig. 5(c) and Table 2. A bimodal particle size distribution is observed

Table 3. Summary of shear-band configurations for solid (prefractured) SiC in different experiments

Material	SiC-I	SiC-II	SiC-III
	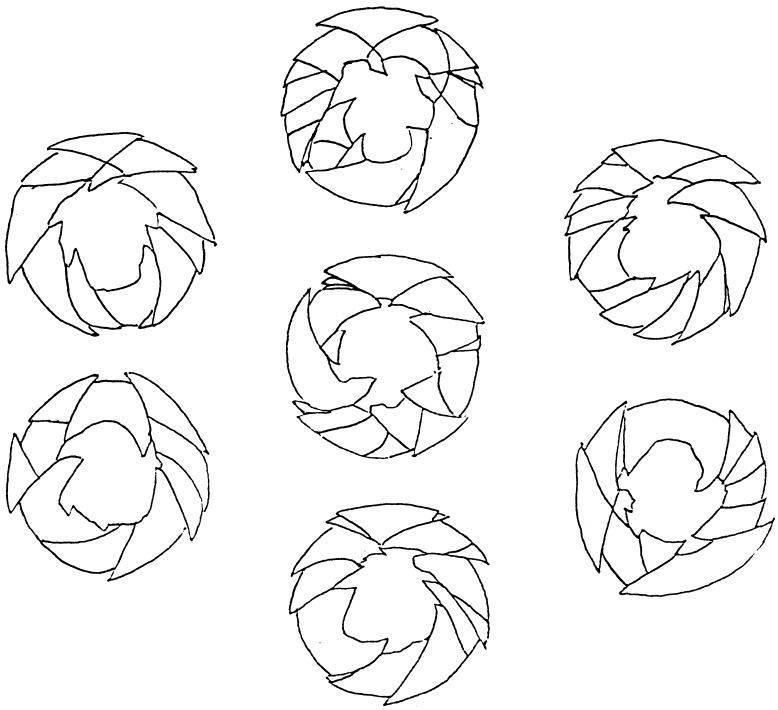		
Number of groups	2 2	2 2 2	2 2
Number of shear bands	11 10	18 17 14	15 11
Average shear-band spacing	2.81 mm 3.05 mm (2.93 ± 0.17 mm)	1.72 mm 1.82 mm 2.18 mm (1.91 ± 0.24 mm)	2.02 mm 2.75 mm (2.39 ± 0.52 mm)
Average displacement	904 μm 910 μm (907 ± 4 μm)	548 μm 561 μm 884 μm (664 ± 190 μm)	669 μm 907 μm (788 ± 168 μm)

inside the shear bands, as shown in Fig. 6(a). The large particles range from 10 to 30 μm, and the small particles vary from 1.5 to 5 μm. The large particles have round corners and contain numerous microcracks, as shown in Fig. 6(b). Outside the shear band, small and large particles can also be identified, as shown in Fig. 6(c). The large particles exhibit the same characteristics as the large particles inside the shear band: round corners and microcracks. These large particles contain characteristic crack patterns, emanating from their contact points (marked by arrows in Fig. 6(c)). Section 3.3 presents an analysis of the stresses within particles subjected to compressive tractions.

Shih *et al.* [26] observed and described in detail the same mechanism in fragmented SiC subject to

Table 4. Deformation during the second explosive event

	Tangential strain	Tangential strain	Average number of bands	Total displacement	Effective strain	Global tangential strain	Shear-band strain	Partition
	$e_{\varphi\varphi}$ at inner radius	$e_{\varphi\varphi}$ at outer radius	N	$\Sigma\Delta$ (mm)	ϵ_{eff}	e_{t}	e_{s}	$e_{\text{s}}/e_{\text{t}}$
Fine powder	−0.349	−0.119	58	1.95	0.281	−0.216	−0.026	0.12
Medium powder	−0.368	−0.098	29	2.82	0.278	−0.214	−0.038	0.18
Coarse powder	−0.358	−0.103	51	0	0.265	−0.205	0	0

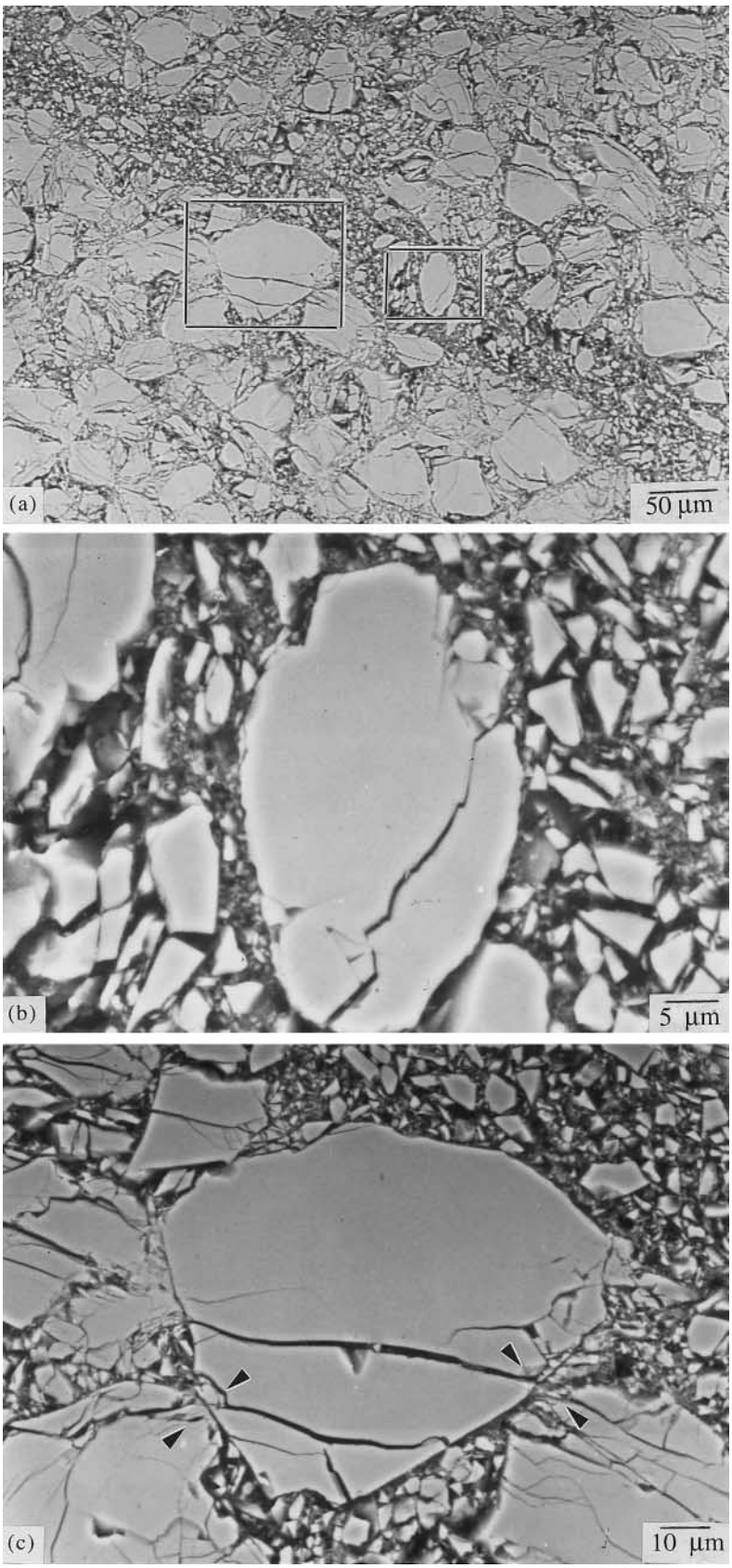

Fig. 6. Shear band of coarse powder: (a) overview; (b) particle inside the shear band; (c) particle at the interface of the shear band.

the similar deformation. Shear-band formation in fragmented silicon carbide is propitiated by comminution of fragments. The comminution proceeds through the incorporation of nearby fragments into the shear band and their erosion inside the shear band. During large deformation, large particles are crushed and broken down, and the resulting small particles can be rearranged to pack more efficiently. The comminution and rearrangement are localized in the shear bands. Recent computer simulation of

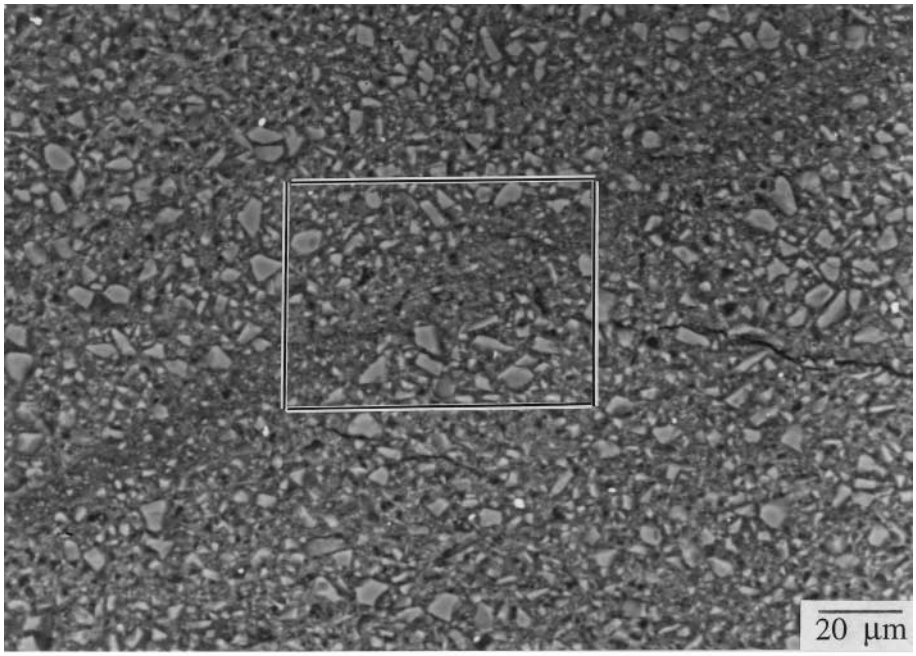

(a)

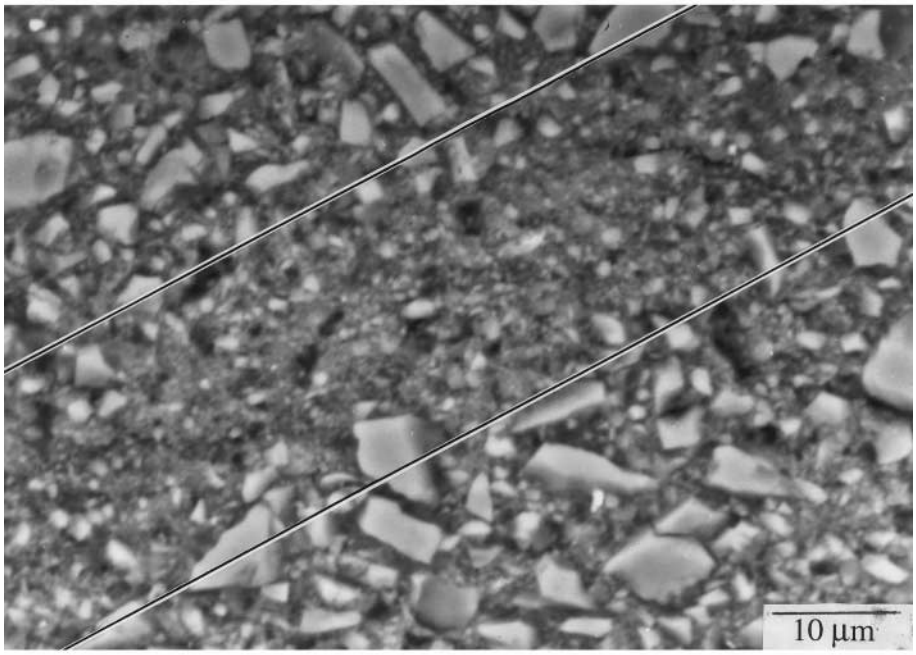

(b)

Fig. 7. Shear band of medium powder with small displacement ($\Delta < 200\ \mu m$, $\gamma_s < 12$): (a) overview; (b) high magnification.

brittle-particle arrays subjected to shear predicts the same mechanism for particle break-up [33]. Since the granular material is porous, the localized comminution and rearrangement are sufficient to accommodate the large strain without the extension of the shear bands. Although the measured shear band strain (e_s in Table 4) is negligible, the deformation is still inhomogeneous in nature. The small displacements in shear bands indicate that they were created during the final stage of the

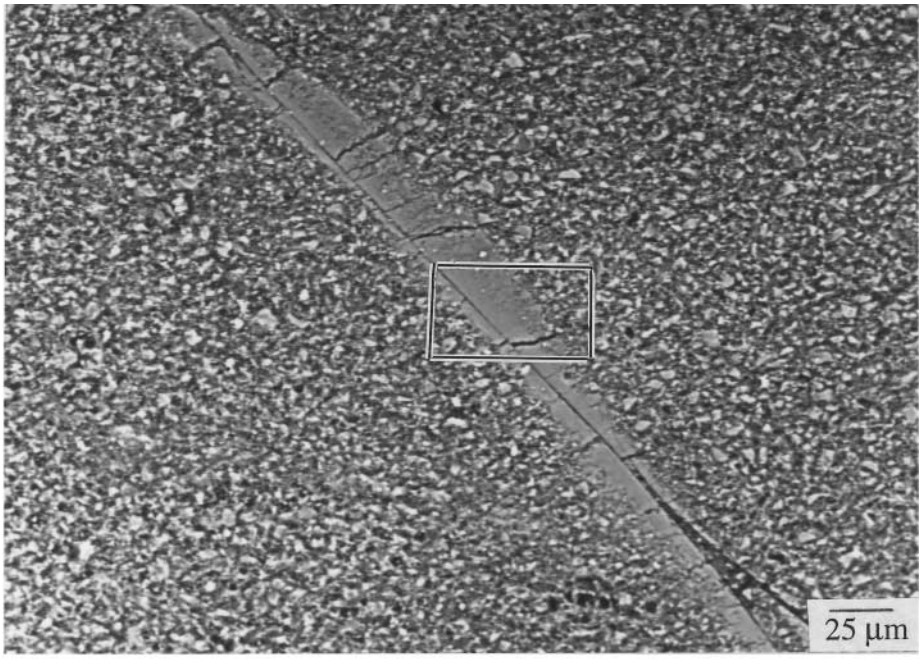

(a)

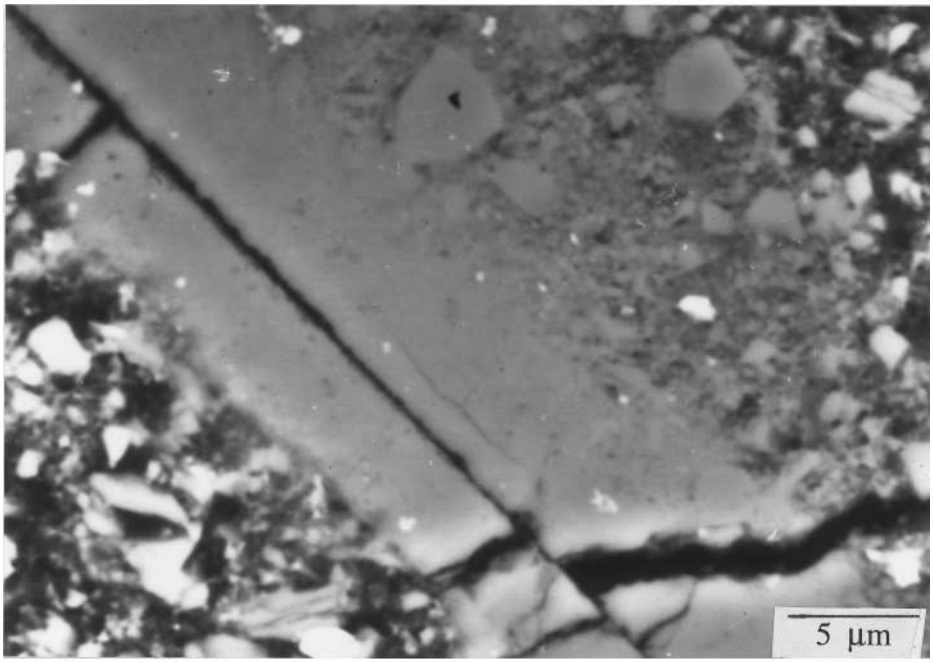

(b)

Fig. 8(a) and (b) (*caption overleaf*).

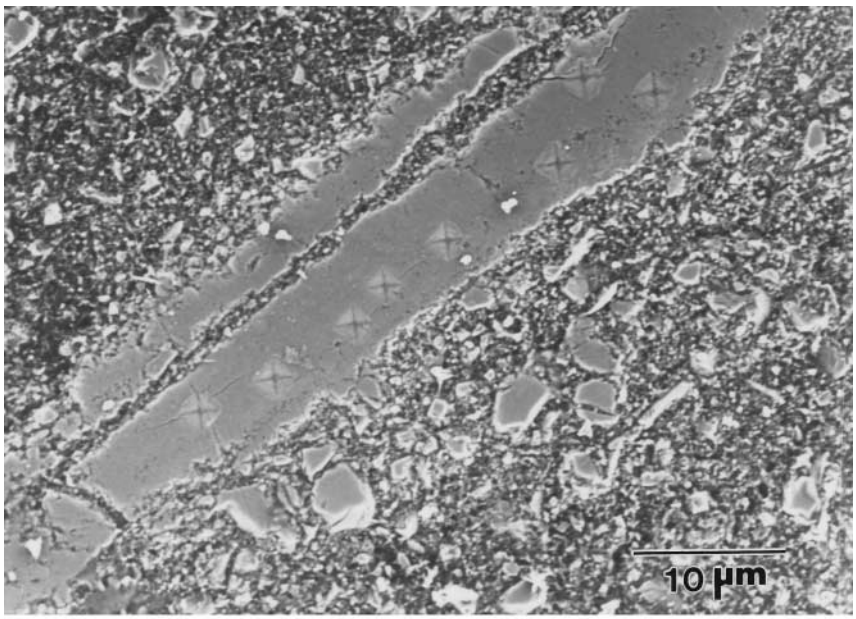

(c)

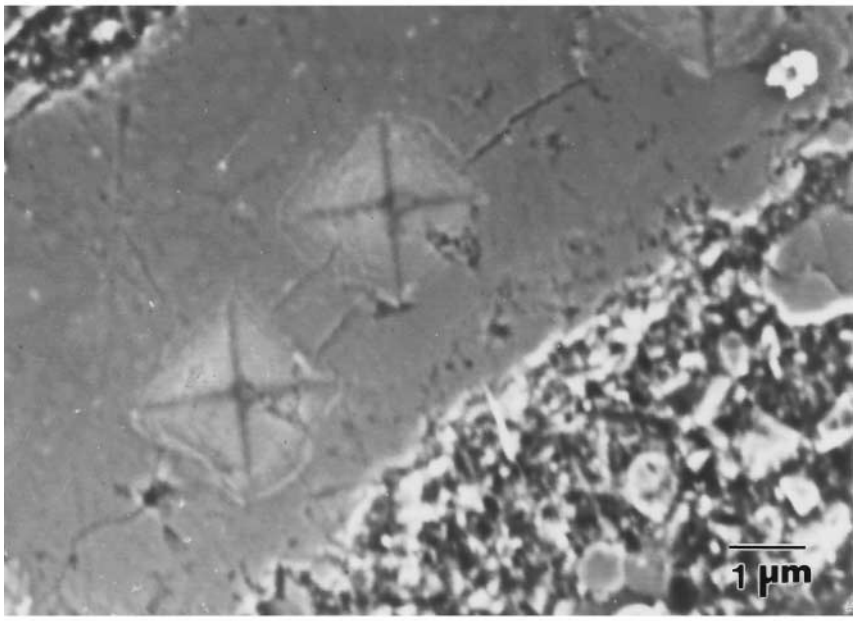

(d)

Fig. 8. Shear band of medium powder with large displacement ($\Delta > 200\ \mu$m, $\gamma_s > 12$): (a) overview; (b) high magnification. Microhardness indentation on the dense SiC layer within the shear band: (c) overview; (d) high magnification.

collapse process; this means that their initiation strain is higher than for the other two granular materials.

3.2.2. Deformation in medium sized granular SiC. This group of specimens had the largest shear-band displacement (Δ), as shown in Table 2. Figure 7 shows a shear band in which comminution occurs. Inside the shear band, there is no particle larger than 1.5 μm, because all large particles have been comminuted. This type of shear band is similar to the shear bands in the coarse powder specimens and in fragmented SiC. However, this comminution phenomenon was observed only in the shear bands with small displacement ($< 150\ \mu$m).

For shear-band displacements larger than 150 μm, a layer of dense SiC along the shear band can be identified, as shown in Fig. 8(a). The density of this SiC layer decreases gradually away from the crack, as shown in Fig. 8(b). It is expected that the large displacement generates local heating. The calculated temperature rise is presented in Section 3.4.

3.2.3. "Sintering" within shear bands. Figures 8(c) and (d) show the micro-indentation markings that were made on the dense SiC layer in the shear

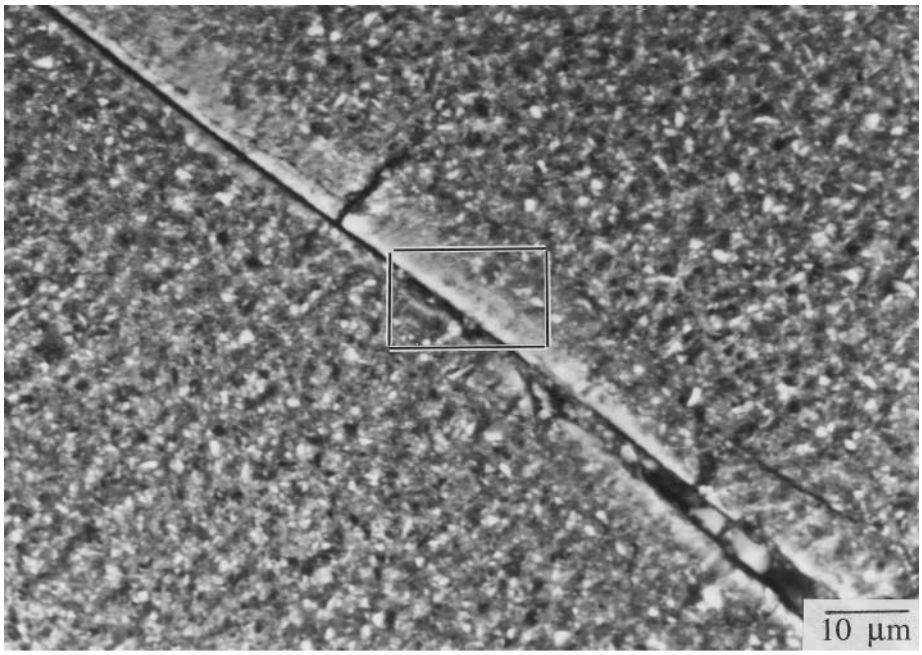

(a)

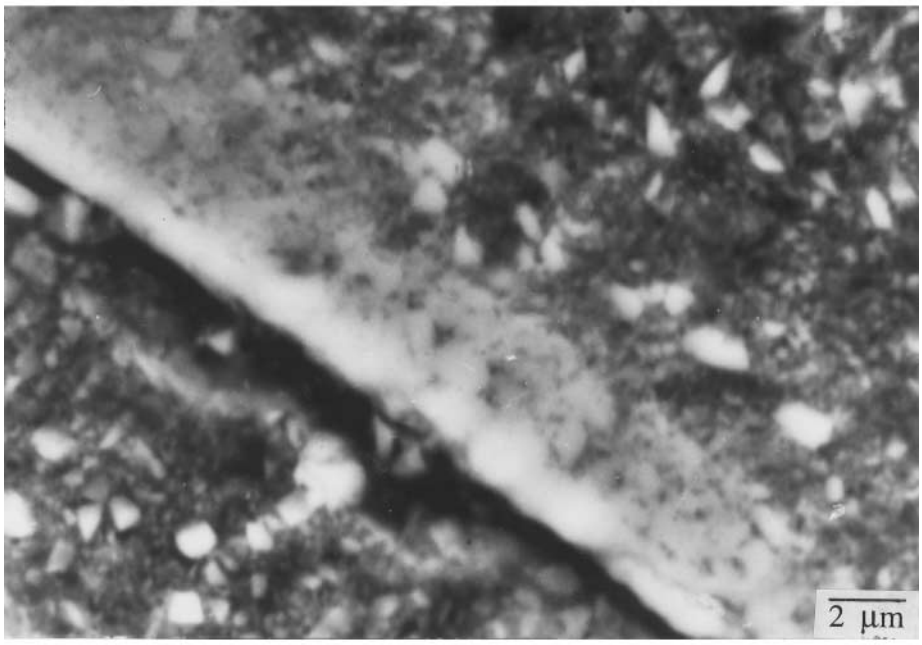

(b)

Fig. 9. Shear band of fine powder with large displacement ($\Delta > 150$ μm, $\gamma_s > 15$): (a) overview; (b) high magnification.

bands. The material did not crumble; on the contrary, the indentation markings are clear and confirm that the powder is fully bonded inside the shear localization regions. The hardness value obtained is 26 GPa, which compares favorably with a reported hardness of 23 GPa for fully dense SiC [26]. The difference could be due to the small load (10 gf) used in the current experiments. It is thought that the strong bonding between the particles, under the influence of high superimposed pressure, is associated with the combined (and coupled) effects of intense plastic deformation and heating, during the shear localization event. This is indeed surprising and is a novel phenomenon, since conventional sintering requires times that are many orders of magnitude higher. The possibility of accelerated diffusion due to the generation of large dislocation densities in the deforming particles should be considered.

3.2.4. Deformation of fine granular SiC. In fine granular SiC, a dense layer of SiC was also identified in shear bands with large displacement ($\Delta > 150\ \mu$m), as shown in Fig. 9. This dense SiC layer was similar to the one observed in the medium powder specimens. If the shear-band displacement was between 100 and 150 μm, only rounded SiC nodules were formed, as shown in Fig. 10. These nodules represent the onset of bonding between the powders, and were also observed in Al_2O_3 granules with 0.4 μm particle size [25]. It is obvious that there is a critical displacement necessary to generate sufficient heat to effect the particle bonding (sintering).

Particle break-up was not activated in fine SiC powders, but pore compaction was identified, as shown in Fig. 11. This is particularly evident for shear bands with low displacement ($\Delta < 100\ \mu$m). The particle size inside the shear band is nearly identical to the particle size outside the shear band. However, the packing density is higher inside the shear band; this is evident by the dark color in the secondary electron SEM images.

3.3. Particle comminution

Granular materials can be represented by close-packed spheres, as shown in Fig. 12(a). The local contact force (F) between spheres is determined by the number of contact points of the spheres, and is directly related to the sphere size (D):

$$F = KPD^2 \tag{4}$$

where P is the external pressure, and K is a dimensionless geometrical factor. Figure 12(b) shows a hexagonal packing of spheres, consisting of numerous unit cells, and represents the top view of a granular material, subjected to a compressive loading. Each unit cell has an area of $\sqrt{3}D^2$, with two effective contact points

$$\left(1 + \frac{1}{4} \times 4 = 2\right).$$

Therefore, one can obtain

$$K = \frac{\sqrt{3}}{2}$$

for the hexagonal packing.

Particles are loaded by the forces applied by all nearest neighbors, and the number of forces per particle is equal to the coordination number. However, there are force chains to transfer the external forces, as shown in Fig. 12(c). The development of the force chains (fabric evolution) has been experimentally examined by Mehrabadi *et al.* [34], and the density of particle contact along the principal stress axes have been demonstrated to approach a constant value during the deformation. Thus, it is appropriate to assume that each particle is loaded by two geometrically opposite forces, as shown in Fig. 12(d). Meyers and Meyers [35] have expressed the maximum tensile stress (σ_t) at the center of the sphere in terms of particle diameter and compressive loads, and have demonstrated that ceramic (iron oxide) spheres fail by axial splitting.

The quantitative prediction of the particle break-up requires an exact estimation of stresses within the particle. Oka and Majima [36] derived an analytical solution for the stress components inside a spherical particle. The results have been examined and corrected by Krosche [37]. The sphere is subjected to a pair of loads concentrated in contact areas, which are defined by the contact angle θ_o, as shown in Fig. 13. Through the elasticity theory and the appropriate boundary conditions (free shear stress at free surfaces), one can derive the stresses generated by the external force (F) as a function of particle diameter (D) [36, 37]:

$$\sigma_r = \frac{2F}{\pi D^2} f_1\left(\theta_0, \nu, \frac{r}{a}, \theta\right) \tag{5}$$

$$\sigma_\theta = \frac{2F}{\pi D^2} f_2\left(\theta_0, \nu, \frac{r}{a}, \theta\right) \tag{6}$$

$$\sigma_\phi = \frac{2F}{\pi D^2} f_3\left(\theta_0, \nu, \frac{r}{a}, \theta\right) \tag{7}$$

$$\tau_{r\theta} = \frac{2F}{\pi D^2} f_4\left(\theta_0, \nu, \frac{r}{a}, \theta\right) \tag{8}$$

$$\tau_{r\theta} = \tau_{r\phi} = \tau_{\theta\phi} = 0 \tag{9}$$

where ν is the Poisson's ratio, a is the radius of the sphere ($a = D/2$), and f_1, f_2, f_3 and f_4 are dimensionless functions, determined by θ_0, ν, r/a and θ. θ_0 is the initial contact angle and θ is the polar coordinate. The full expressions are given in the Appendix A. Substituting equation (4) into equations (5)–(8), one can find that the stresses in the particles are determined by the pressure (P), and independent of

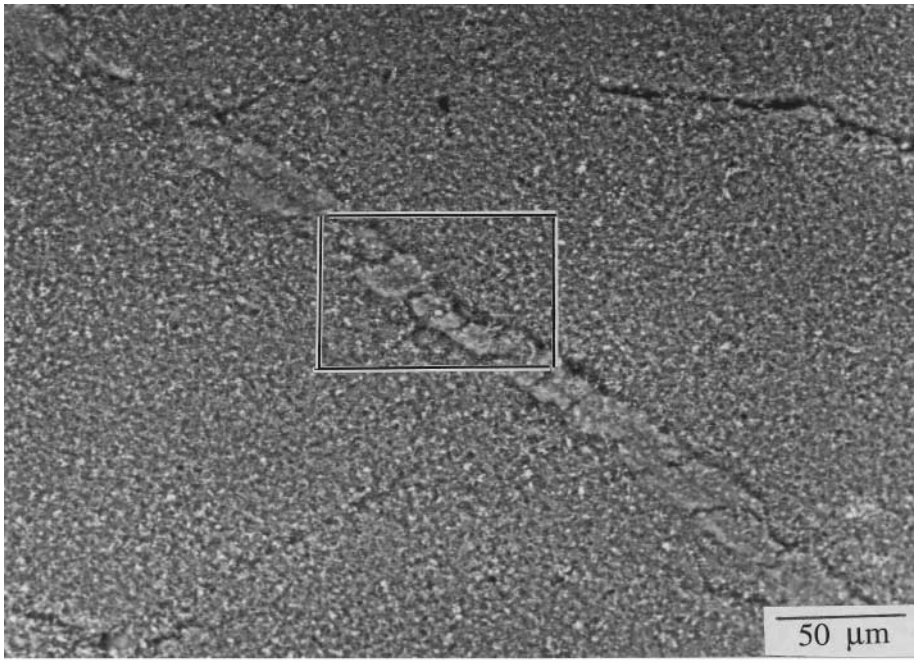

(a)

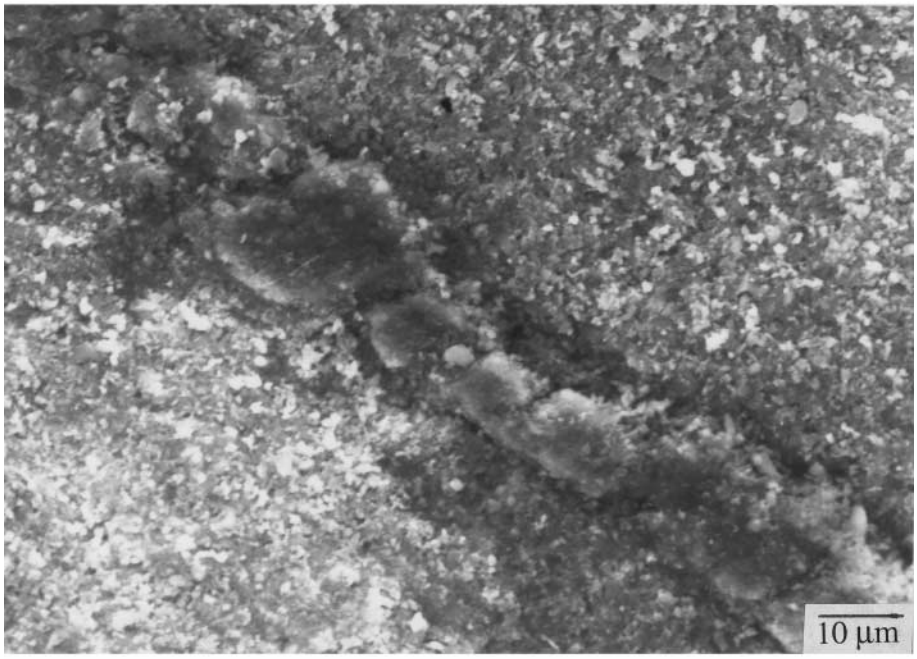

(b)

Fig. 10. Shear band of fine powder with medium displacement (Δ = 100–150 μm): (a) overview; (b) high magnification.

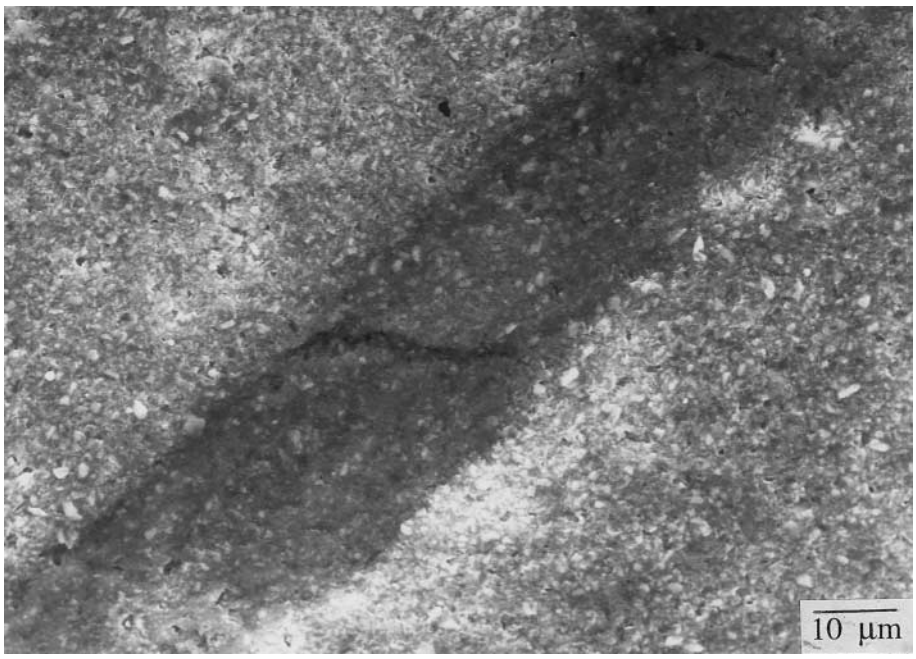

Fig. 11. Pore compaction in shear band of fine powder with small displacement ($\Delta < 100\ \mu$m).

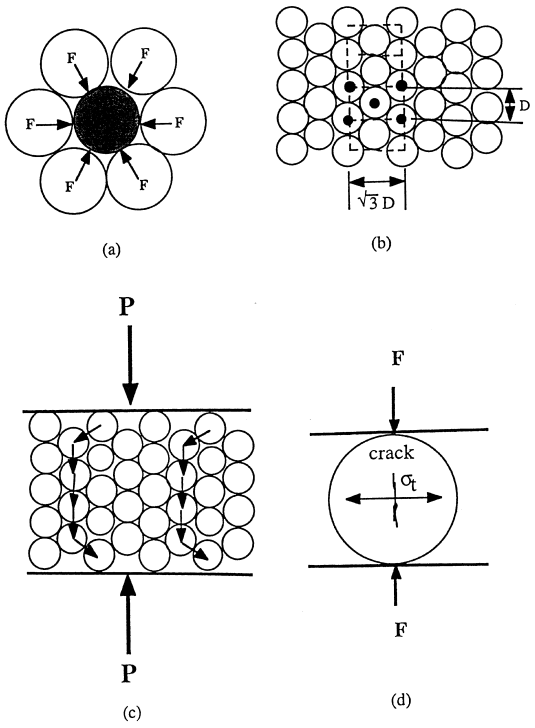

Fig. 12. Comminution: (a) particle subjected to forces from neighboring particles; (b) a granular material with hexagonal close packing; (c) chains of force; (d) tensile fracture in a particle subjected to compression.

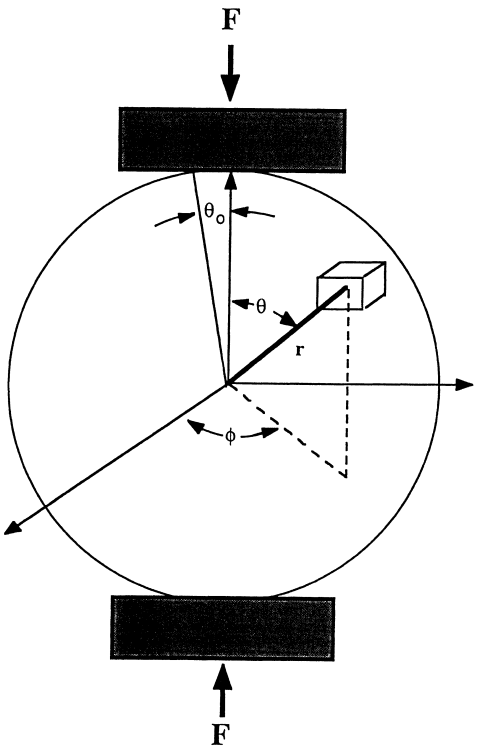

Fig. 13. Coordinates of a sphere under a pair of concentrated loads.

the particle size:

$$\sigma_r = \frac{2K}{\pi} \cdot f_1\left(\theta_0, \nu, \frac{r}{a}, \theta\right) \cdot P$$

$$\sigma_\theta = \frac{2K}{\pi} \cdot f_2\left(\theta_0, \nu, \frac{r}{a}, \theta\right) \cdot P \tag{10}$$

$$\sigma_\phi = \frac{2K}{\pi} \cdot f_3\left(\theta_0, \nu, \frac{r}{a}, \theta\right) \cdot P \tag{11}$$

$$\tau_{r\theta} = \frac{2K}{\pi} \cdot f_4\left(\theta_0, \nu, \frac{r}{a}, \theta\right) \cdot P. \tag{12}$$

Through the stress components, principal stresses (σ_1, σ_2 and σ_3) can be calculated using invariants. It is convenient to define the normalized principal stresses (Φ_1, Φ_2 and Φ_3) as:

$$\Phi_1 = \frac{\pi}{2K}\frac{\sigma_1}{P} \tag{13}$$

$$\Phi_2 = \frac{\pi}{2K}\frac{\sigma_2}{P} \tag{14}$$

$$\Phi_3 = \frac{\pi}{2K}\frac{\sigma_3}{P}. \tag{15}$$

The Poisson's ratio of SiC is 0.17, and the contact angle (θ_o) is assumed to be 10° for the calculation. This is a reasonable approximation for inter-particle contact angle. As shown in Fig. 14, Φ_1 and Φ_2 are tensile in the interior of the sphere, and Φ_3 is always compressive. Polar, iso-stress representations for Φ_1, Φ_2 and Φ_3 are shown in Fig. 15. The compression regions for Φ_1 and Φ_2 are localized around the contact points. The transition from tension to compression ($\Phi_1 = \Phi_2 = 0$) is shown in Fig. 16(a). It is clear that Φ_1 has a larger tension region than Φ_2. For the sake of describing the failure of the sphere, it is necessary to define the tension and compression regions. The following assumptions are made: (i) if one of the principal stresses is tensile, the fracture is tensile; (ii) fracture is compressive if all three principal stresses are compressive. Since the magnitude of the compression stresses of Φ_2 around $\theta = \pm 90°$ is very small [see Fig. 14(b)], the overall tension/compression boundary is defined by the contour of Φ_2 around the contact points ($\theta = 0$ and 180°), as shown in Fig. 16(b). By integrating, one can derive that the volume fraction of compression region (V_C) is about 0.078, and the volume fraction of tension region (V_T) is around 0.922.

As shown in Fig. 14, the magnitudes of Φ_1, Φ_2 and Φ_3 decrease as the coordinate angle (θ) increases. It is concluded that the loading axis (at $\theta = 0°$) is the most critical direction for fracture. The values of Φ_1, Φ_2, and Φ_3 along the loading axis are plotted in Fig. 17(a). At $\theta = 0°$, Φ_1 and Φ_2 are identical, i.e. $\Phi_1 = \Phi_2$. Therefore, along the loading axis, the stress components can be simplified using a two-dimensional representation, as plotted in Fig. 17(b).

Griffith derived a failure criterion, based on an inclined crack subjected to two principal stresses, as shown in Fig. 18 [38]. Localized tensile stresses, induced by the compressive tractions, cause crack propagation. The failure criterion is as follows:

$$\sigma_1 = \sigma_3 = \sigma_T \text{ for } 3\sigma_1 + \sigma_3 > 0 \tag{16}$$

$$(\sigma_1 - \sigma_3)^2 + 8\sigma_T(\sigma_1 + \sigma_3) = 0 \text{ for } 3\sigma_1 + \sigma_3 < 0 \tag{17}$$

where σ_T is the uniaxial tensile strength. The failure criterion is graphically shown in Fig. 19. A material is considered failed if the stress conditions are outside the stress envelope. Although this is a simplified criterion, which has been superseded by more advanced treatment incorporating friction between the crack surfaces and other considerations (e.g. McClintock and Walsh [39]), the Griffith criterion predicts a realistic relationship between the tensile and compressive strength of brittle materials: $\sigma_C = 8\sigma_T$.

In order to apply the Griffith criterion to the stresses inside the sphere, a mathematical manipulation is required. Assuming the first principal stress [σ_1 in equation (13)] is equal to the tensile fracture strength (σ_T) fracture, one can obtain:

$$\sigma_T = \frac{2K}{\pi}\Phi_m P_T \tag{18}$$

P_T is the critical pressure on the granular material required for tensile fracture of the particle, and Φ_m is the maximum of the normalized principal stress (Φ). As shown in Fig. 14, the maximum principal tensile stress (Φ_m) is 1.70. The following two equations can then be easily established:

$$\frac{\sigma_1}{\sigma_T} = \frac{P}{P_T}\frac{\Phi_1}{\Phi_m} \tag{19}$$

$$\frac{\sigma_3}{\sigma_T} = \frac{P}{P_T}\frac{\Phi_3}{\Phi_m}. \tag{20}$$

Fig. 20(a) shows the ratios σ_1/σ_T and σ_3/σ_T at different P/P_T. At small pressure (P), the stresses are within the envelope and the particle will not fail. As P increases, tensile or compressive failure will occur. As shown in Fig. 20(b), the compressive failure would be initiated at $r/a = 0.8$ when:

$$P \approx \frac{1}{3}P_T = \frac{\pi}{6K\Phi_m}\sigma_T = \frac{\pi}{48K\Phi_m}\sigma_C \tag{21}$$

where σ_T and σ_C are the tensile and compressive strength, respectively ($\sigma_C = 8\sigma_T$). This equation implies that the critical pressure for particle failure is only determined by the strength, and independent of the particle size. However, strength of a brittle ceramic is strongly influenced by the volume. Larger particles have more flaws and lower strength, and the Weibull statistics can accurately

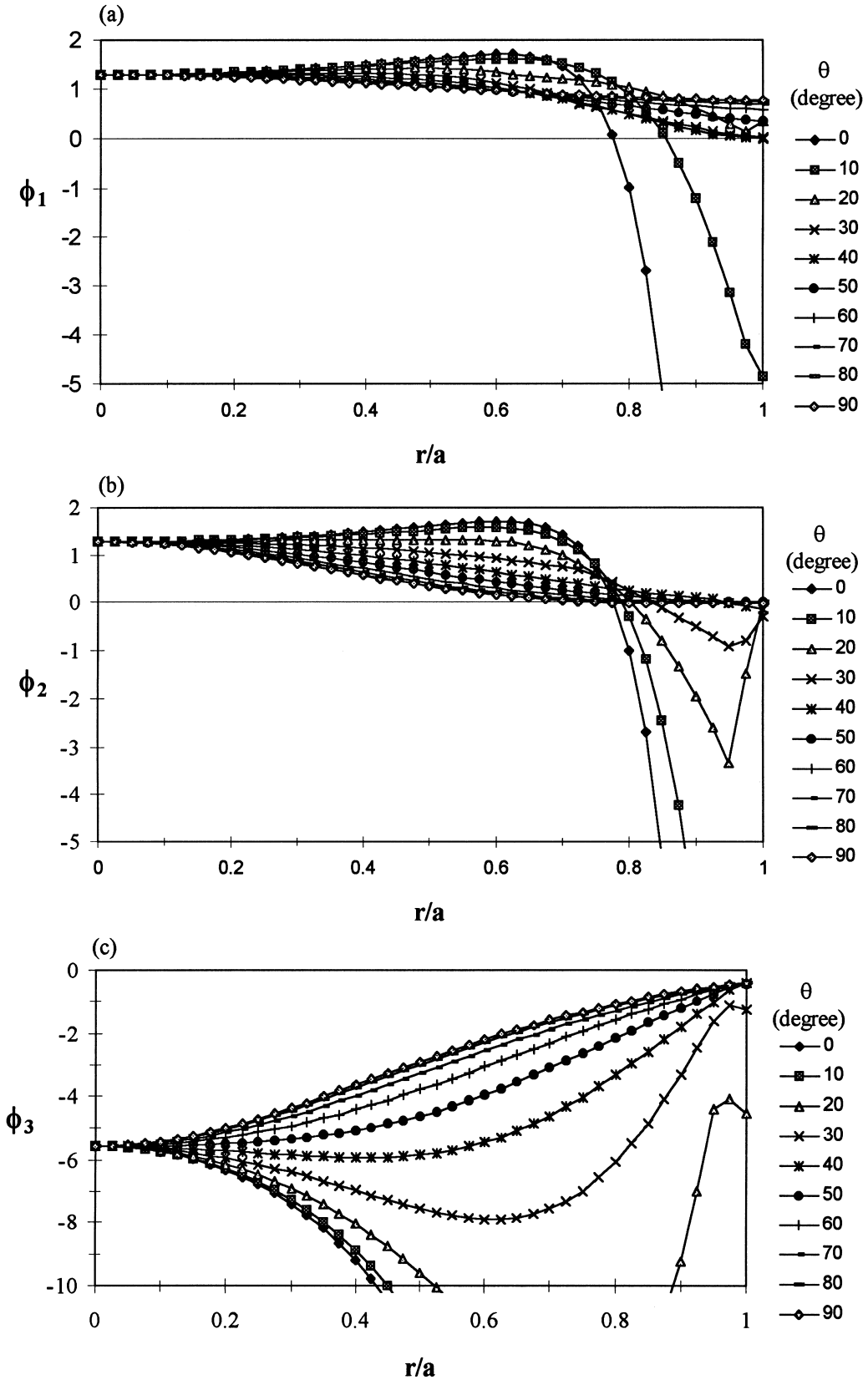

Fig. 14. Normalized principal stress as a function of distance (r) and angle (θ): (a) Φ_1; (b) Φ_2; (c) Φ_3.

describe the size effect [40]:

$$P_f = 1 - \exp\left(- kV \left(\frac{\sigma}{\sigma_o} \right)^m \right) \tag{22}$$

where P_f is the probability of failure under a tensile stress σ, k is a loading factor, V is the volume under stress, m is the Weibull modulus and σ_o is a normalization parameter. The load factor (k) is dimensionless, and is unity for tension. The product kV is often referred to as the effective stressed volume. Since the volume is directly related to the particle size (D), the strength of different particles can be related as follows:

$$\frac{\sigma_2}{\sigma_1} = \left(\frac{k_2}{k_1} \right)^{-\frac{1}{m}} \left(\frac{D_2}{D_1} \right)^{-\frac{3}{m}} \tag{23}$$

where σ_1 and σ_2 are the strength of the particle with the diameter of D_1 and D_2, and load factor of

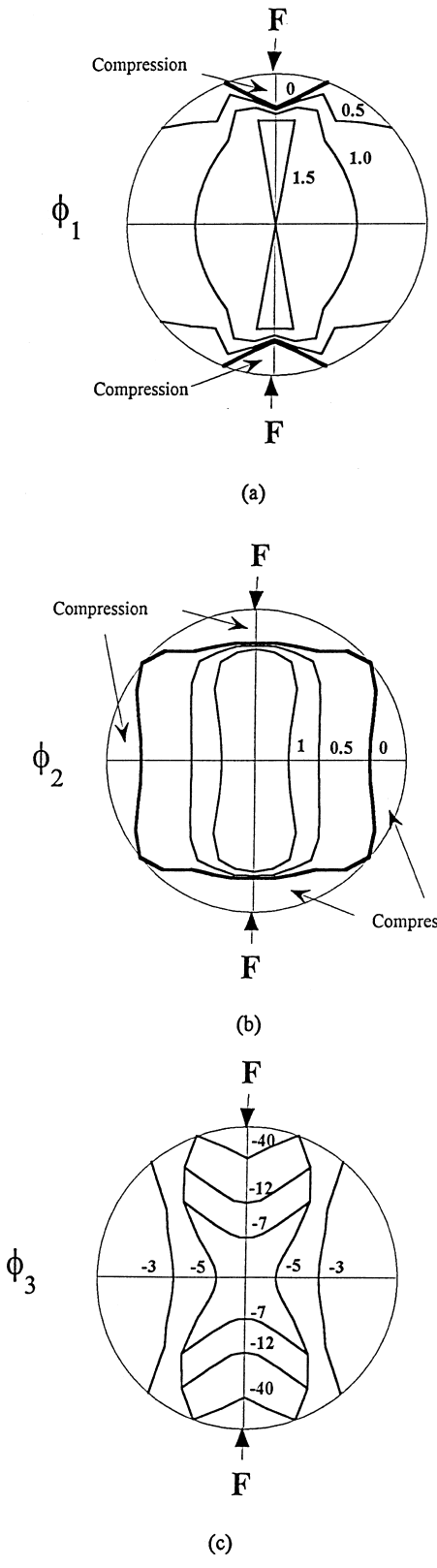

Fig. 15. Polar presentation of normalized principal stresses: (a) Φ_1; (b) Φ_2; (c) Φ_3.

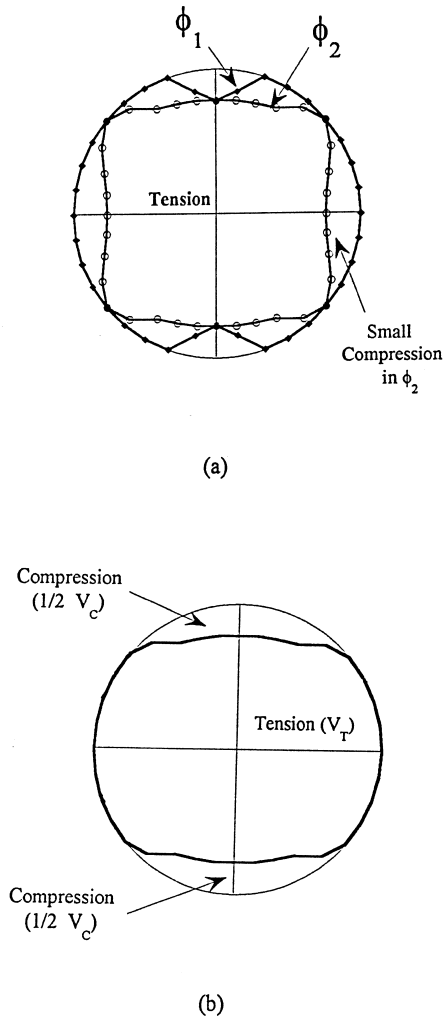

Fig. 16. Polar presentation: (a) tension/compression transition in Φ_1 and Φ_2; (b) tensile and compressive domains inside the particle.

k_1 and k_2, respectively, under the same probability of failure. Shih and Ezis measured the tensile strength of hot-pressed SiC, and reported the average tensile strength of 497 MPa, and Weibull modulus of 10 [41]. The gage section of the specimens was 6.35 mm in diameter and 35 mm long, volume corresponding to a sphere of 12.8 mm diameter. Therefore, equation (23) can be directly applied to the particle comminution, using the following parameters: $\sigma_1 = 497$ MPa, $k_1 = 1$, $m = 10$, and $D_1 = 12.8$ mm.

The particle is stressed by both tension and compression, and both particle size (D) and load factor (k) should be taken into consideration. As shown in Fig. 16(b), approximately 7.8% of the volume is considered under compression. The load factor [k_2 in equation (23)] is directly related to the volume fraction of tension (V_T) inside the particle to describe the critical external pressure for tension failure (P_T); P_T is obtained from equations (18) and (23) by making $k_2 = V_T$:

$$P_T = \frac{\pi}{2K\Phi_m}\left(\frac{V_T^{\frac{1}{3}}\sigma_1}{D_1}\right)^{-\frac{3}{m}}. \tag{24}$$

As shown in Fig. 20(b), the critical external pressure for compression failure (P_C) is one third of the one for tensile failure; therefore, one can obtain, by making $k_2 = V_C$:

$$P_C = \frac{P_T}{3} = \frac{\pi}{6K\Phi_m}\left(\frac{V_C^{\frac{1}{3}}\sigma_1}{D_1}\right)^{-\frac{3}{m}} \tag{25}$$

where the volume fraction of compression (V_C) replaces the volume fraction of tension (V_T) to describe the change in loading condition. Equations (24) and (25) are graphically represented in Fig. 21. It is obvious that the compression failure occurs much earlier than the tensile failure. Since the compressive region is much smaller than the tensile

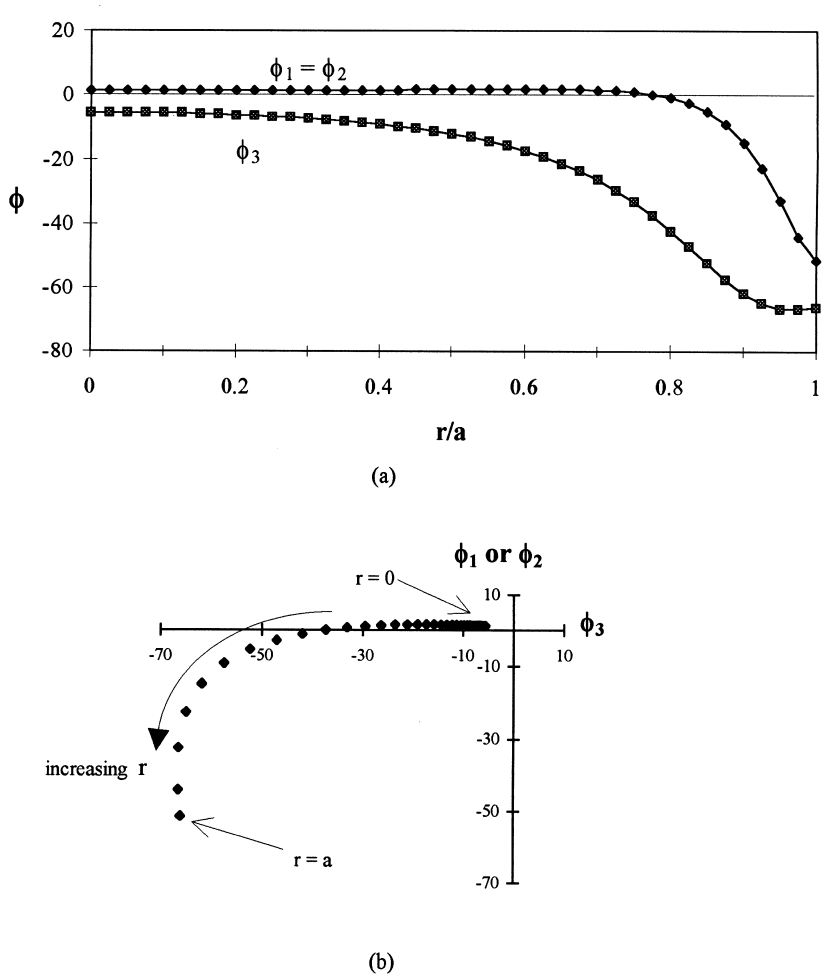

Fig. 17. Principal stresses along the loading axis ($\theta = 0°$): (a) Φ_1 and Φ_3 as a function of distance from the center; (b) Φ_1 vs Φ_3.

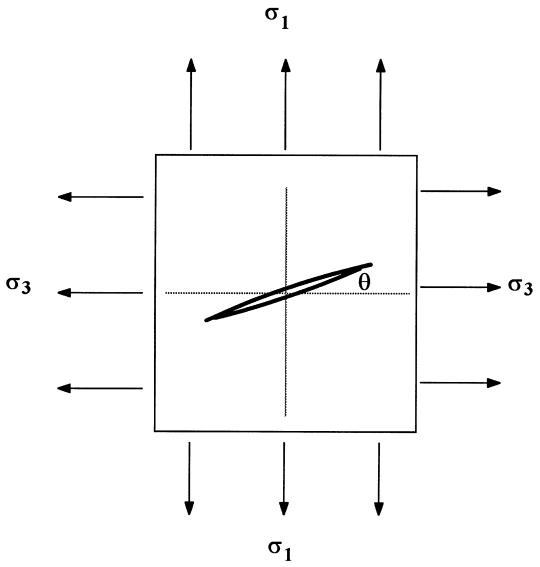

Fig. 18. Schematic diagram of an inclined crack under biaxial loading.

region, it is expected that cracks originate in the compression region, readily penetrate into the main body of the sphere, subjected to tension. This leads to the well-known axial splitting of the sphere, dictated by σ_1. The cracks are characteristically parallel to the loading direction [Fig. 6(c)].

A very important conclusion can be derived from the analysis: the external pressure required to fracture the particles is strongly dependent on their diameter. Figure 21 shows that the pressures are 1.2, 2.8 and 5.1 GPa for the 50, 3 and 0.4 μm particle sizes, respectively. This calculation predicts a fourfold increase in the pressure required to fracture the particles as their size is reduced by two orders of magnitude, and is in full accord with the observations. The coarse powders (50 μm) were comminuted to small pieces during the large strain, high-strain-rate deformation, and the particle break-up was never seen in the fine powders (0.4 μm).

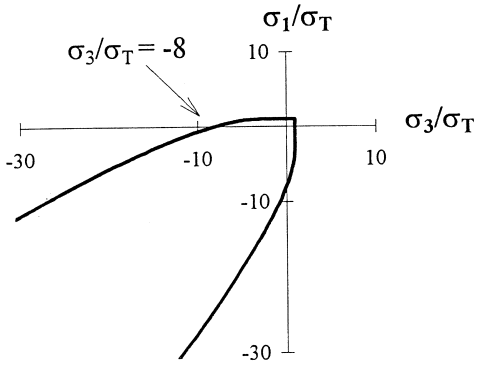

Fig. 19. Schematic representation of brittle failure using Griffith criterion.

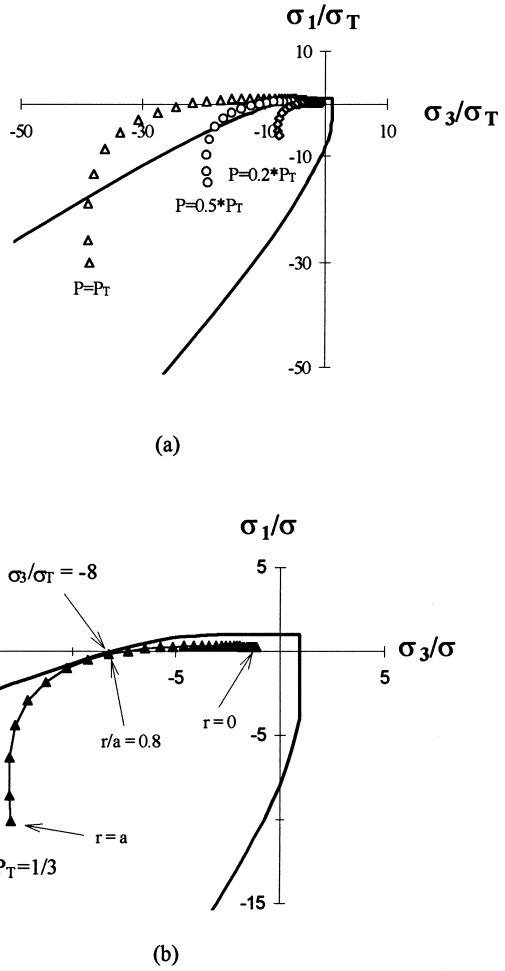

Fig. 20. Principal stresses inside a particle: (a) with increasing pressure (P); (b) compressive at $r/a = 0.8$, when $P = 1/3P_T$.

The analysis is based on the assumption that failure is governed by the maximum principal stresses. For the tensile region, σ_1 dictates failure; while in the compression region, the combination of σ_1 and σ_3 determines the fracture. Lateral confinement has been demonstrated to play a critical role in crack evolution [42, 43]. This model does not include the confinement effect since only two forces per particle are used, and is derived to demonstrate the influence of particle size on the particle comminution.

3.4. Temperature rise in shear localization regions

In the thick-walled cylinder experiments, a lateral confinement is generated by the kinematics of the convergent geometry that creates compressive tangential stresses. Under lateral confinement, shear localization is a favored deformation mechanism of granular materials, to bypass the dilatation that would occur for large homogeneous granular flow [25, 26].

A model geometry for the kinetics of shear localization can be schematically represented in Fig. 22,

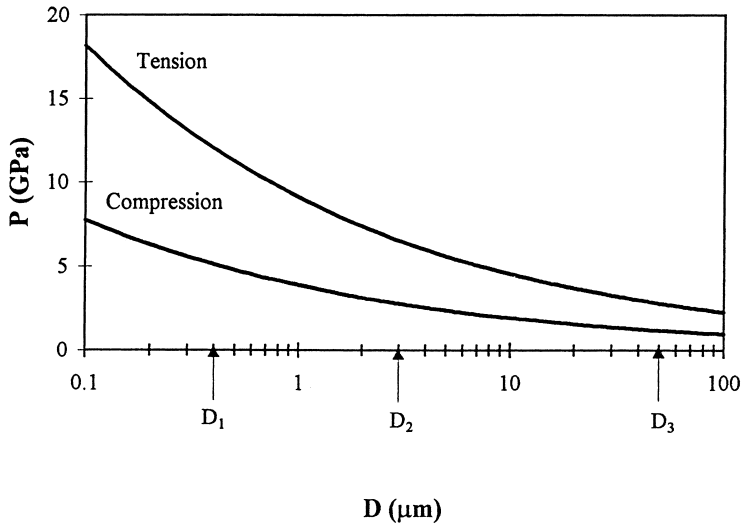

Fig. 21. Relationship between external pressure and particle size through tensile and compressive fracture.

where S is the spacing between the shear bands, and w is the width of the shear band. During the formation of shear bands, the plastic deformation and inter-particle friction generate heat. Inside the shear band, the temperature with respect to time (t) and location (x) can be described through an energy balance:

$$\frac{\partial}{\partial t}(\rho C_p T) = k\frac{\partial^2 T}{\partial x^2} + K_{ph}\tau\frac{\partial \gamma}{\partial t} \tag{26}$$

where ρ is the density, C_p is the specific heat, T is the temperature, k is the heat conductivity, K_{ph} is the coefficient describing the efficiency of transformation of plastic work into heat, and τ and γ are the shear stress and shear strain of the granular SiC.

The engineering shear strain of the granular SiC can be approximated by the shear-band strain (γ_s), which can be directly measured:

$$\gamma_s = \frac{\Delta}{w} \tag{27}$$

where Δ is the shear-band displacement, and w is the thickness of the shear band. The shear stress during the large deformation is assumed to be the same as the shear strength, which is a strong function of temperature. As the temperature increases, the shear strength decreases through thermal softening. To date, there is no available literature data of shear strength of SiC, and certain assumptions are needed for approximation. The phase diagram of SiC presented by Massalski and Abbaschian [44]

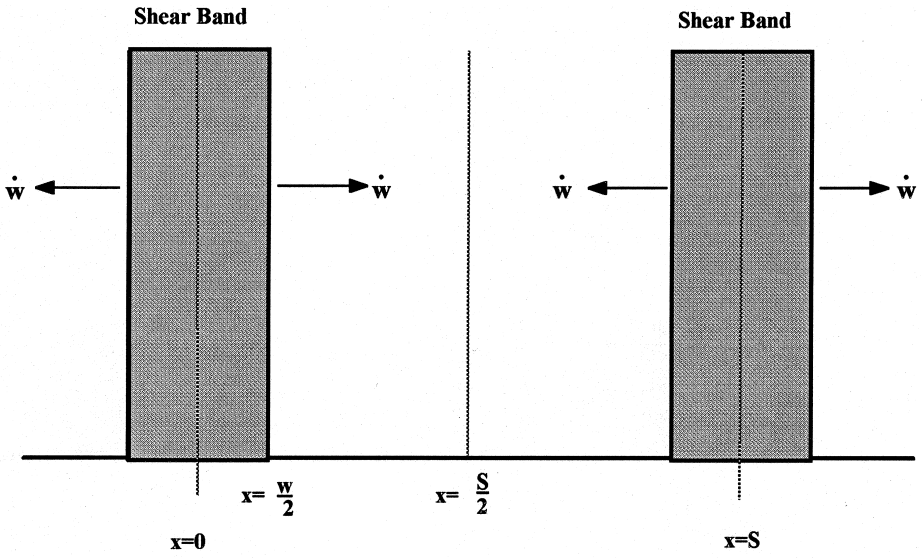

Fig. 22. Schematic one-dimensional diagram for shear-band propagation.

indicates a peritectic transformation of SiC at 2545 ± 40°C, and it is reasonable to assume a zero shear strength at 2545°C. Srinivasan [45] demonstrated that sintered SiC retained its flexural strength until 1600°C. Therefore, a bilinear relationship is proposed to describe the shear strength of SiC:

$$\tau = \tau^* \quad \text{for } T < 1600^\circ\text{C} \tag{28}$$

$$\tau = \tau^* \left(1 - \frac{T - 1600}{945}\right) \quad \text{for } 1600^\circ\text{C} < 2545^\circ\text{C} \tag{29}$$

where τ^* is the shear strength at temperatures below 1600°C, as shown in Fig. 23. It is assumed that the shear strength is half of the uniaxial compressive strength. Lankford reported the compressive strength of 3.8 GPa for sintered SiC [46]. Therefore, τ^* is taken as 2 GPa.

It is assumed that the granular material does not work harden, under the imposed conditions. There is only scant experimental evidence on the high-strain-rate response of granular ceramics under superimposed pressure. Klopp and Shockey [22] proposed a much more general expression for the shear strength of granular material:

$$\tau_y = F(P, \overline{D})\tau_{yo} + \frac{h}{3}\bar{\gamma}^p \tag{30}$$

where F is the mean stress-damage function, P is the pressure, $\overline{D}$ is a damage parameter (varying between 0 and 1), τ_{yo} is the initial shear strength at atmospheric pressure, h is the tangent modulus of a uniaxial stress–strain curve, and $\bar{\gamma}^p$ is the plastic shear strain. Sundaram [47] proposed an expression for the shear flow stress, based on the Mohr–Coulomb model:

$$\tau_y = \mu P + (1 - \mu)\rho d^2 \dot{\gamma}^2 \tag{31}$$

where τ_y is the shear stress, μ is the internal friction coefficient, ρ is the density, d is the particle size in the granular material, and $\dot{\gamma}$ is the shear strain rate. The shear flow stress of a granular material is then

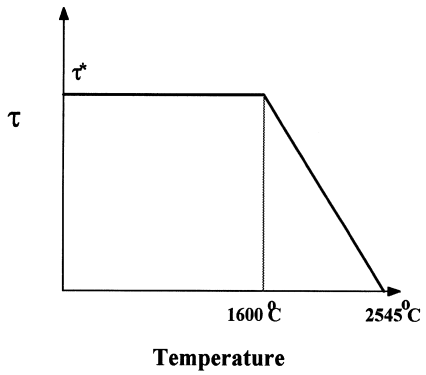

Fig. 23. Hypothetical constitutive response of SiC incorporating thermal softening.

related to the friction effect (rate-independent) and the collision effect (rate-dependent). For strain rates less than 10^5/s, the collision effect is negligible. Klopp and Shockey [22] obtained the shear stress of fractured SiC, which was comminuted from a solid SiC in the first stage (1 ns) of the experiment, and reported the internal friction coefficient of 0.23. However, the authors expressed uncertainty about the results, because of the concern in the control of wave propagation and slip between impact plates. Rudnicki and Rice [48] measured the friction coefficient between 0.4 and 0.9 using a mineral-on-mineral sliding technique. The friction coefficient of precomminuted SiC was 0.45 under quasistatic conditions, as reported by Johnson *et al.* [49]. The recent results, by Sairam and Clifton [50], show no strain hardening in granular Al_2O_3, and the friction coefficient was reported as 0.20 for the granular Al_2O_3, made up of 0.4 μm powder. The friction coefficient appears to increase slightly by increasing pressure and decreasing porosity [47]. In addition, plastic deformation of Al_2O_3 particles was observed under small lateral constraint. Sundaram [47] also examined the granular SiC using 4 μm powder with 40% of packing density, and its friction coefficient is 0.18. All these works indicate that the flow stress of a granular material is strongly dependent on the pressure.

The thick-walled cylinder experiments of this investigation are a strain-controlled technique, and the stress system is not sufficiently well characterized. As shown in Figs 7 and 8, the comminuted particles are about 1.5 μm, and the stress calculation (Fig. 21) indicates that the normal pressure for breaking 1.5 μm particles is around 4 GPa, which is similar to the quasistatic compressive strength of solid SiC [46]. Since the granular materials are confined by the material inertia, the pressure required to comminute particles would be substantially higher than 4 GPa. If the Hugoniot Elastic Limit is considered as the stress to break up the particles under high strain rate with confinement, the shear stress can be estimated as follows:

$$\tau_y = 0.18 \times \text{HEL} = 2.7 \text{ GPa} \tag{32}$$

where HEL is the Hugoniot Elastic Limit of SiC, reported as 15 GPa by Grady [51]. Therefore, the assumed value for τ^* (2 GPa) is appropriate.

The choice of value for τ^* (2 GPa) will affect the calculation for the temperature profile in the shear bands. Nevertheless, the choice is very conservative, since it is based on interparticle sliding, as discussed above. If plastic deformation of the individual particles is being carried out, the shear stress can be much higher:

$$\tau_y = \frac{\text{HEL}}{2} = 7.5 \text{ GPa}. \tag{33}$$

Considering temperature-independent ρ, C_p and k, the heat transfer inside the shear band can then be

expressed as the following equation:

$$\rho C_p \frac{\partial T}{\partial t} = k \frac{\partial^2 T}{\partial x^2} + K_{ph} \tau \frac{\partial \gamma_s}{\partial t}. \quad (34)$$

Outside the shear band, the deformation of SiC particles is negligible, and the heat transfer is expressed as follows:

$$\rho C_p \frac{\partial T}{\partial t} = k \frac{\partial^2 T}{\partial x^2}. \quad (35)$$

In the thick-walled cylinder experiments, the strain rate is approximately 3×10^4/s, and the deformation is completed within 7 μs. We assume that the thickening (propagation) of the shear band is carried out under a constant speed:

$$\dot{w} = \frac{w_f}{t_s} \quad (36)$$

where $\dot{w}$ is the shear-band thickening velocity, w_f is the final shear-band thickness and t_s is the total time for the deformation ($t_s = 7$ μs). At a specific time t, the shear-band boundary is calculated as $x = \dot{w}t$.

The initial and boundary conditions for this heat-transfer equation are as follows:

$$\text{At } t = 0,\ T = 25^\circ\text{C} \quad (37)$$

$$\text{At } x = 0,\ \frac{\partial T}{\partial x} = 0 \quad (38)$$

$$\text{At } x = \frac{S}{2},\ \frac{\partial T}{\partial x} = 0. \quad (39)$$

A numerical calculation using the finite difference method was performed using the following material constants, representing the deformation of granular SiC exhibiting a dense SiC layer inside the shear band: ρ = 2700 kg/m^3 (85% dense); C_p = 1200 J/kg-K; k = 40 W/m-K; γ_s = 12; S = 1 mm; K_{ph} = 1; and w_f = 25 μm. The calculated temperature at the center of the shear band are shown in Fig. 24. The temperature rises at an approximately constant rate until t_s. The maximum temperature is about 2300°C. After t_s, the temperature decreases rapidly through heat conduction. Temperature profiles before t_s and after t_s are shown in Figs 25(a) and (b), respectively.

As a covalently bonded material, SiC is very difficult to densify. The typical processing temperature for SiC using hot pressing or hot isostatic pressing is around 2000°C. As shown in Fig. 25, at t_s, the calculated temperature is above 2000°C at which $x < 8$ μm. In other words, there is a 16 μm thick zone undergoing heating above 2000°C. The thickness of the dense SiC layer (Fig. 8) is about 12 μm, which corresponds reasonably well with the numerical calculation.

As described in Section 3.2, the thin, dense SiC layers were present in the shear bands with large displacement. The driving force for the heat-up process is inter-particle friction and plastic deformation of SiC, and a large shear-band displacement is the necessary condition. During the large strain deformation, coarse SiC powders are prone to break up into small pieces, and the shear deformation is clearly not activated. On the other hand, the shear localization of fine granular SiC can be carried out through pore compaction, resulting in small shear-band displacement. Only the medium SiC powders exhibit sufficient shear deformation, and show profuse evidence for the pressure-sintering mechanism.

The deformation mechanisms influence the efficiency of converting plastic work to heat (K_{ph}). Large particles have more flaws and tend to fracture, and part of the plastic deformation is dissipated through fracture to create new surface, leading to small conversion from plastic work to heat ($K_{ph} < 1$). The calculation for the temperature profile used the assumption of complete energy conversion ($K_{ph} = 1$) to demonstrate the effect of plastic work to local heating, mainly for the medium and fine granular materials.

It should be noted that a similar bonding process of comminuted particles has been recently observed

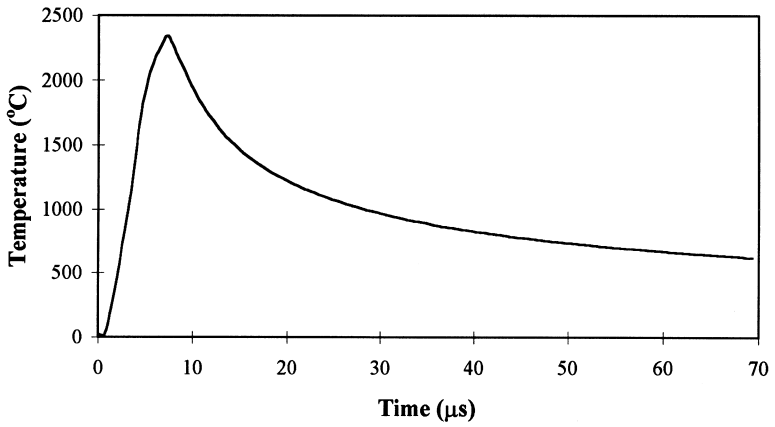

Fig. 24. Calculated temperature at the middle of the shear band.

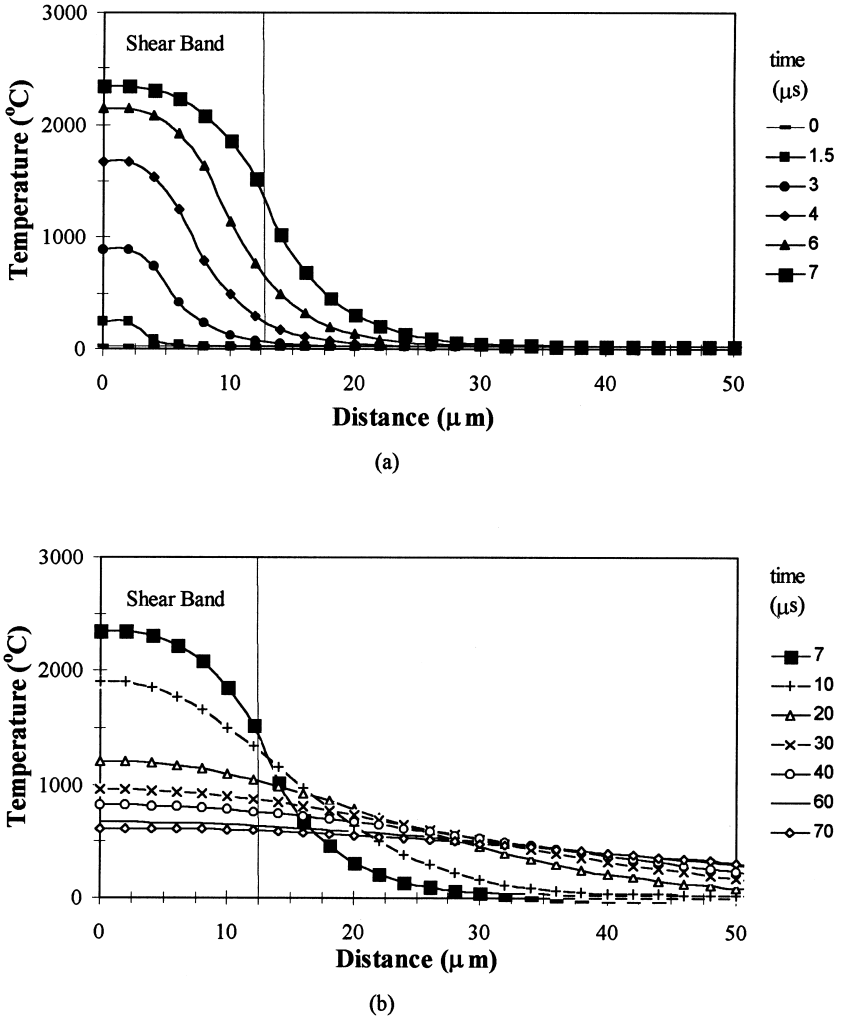

Fig. 25. Calculated temperature profile: (a) during shear-band formation; (b) after completion of shear-band propagation.

during ballistic testing [52, 53]. To date, there is no study to correlate this bonding process with the ballistic performance of the ceramic armor system yet. Nevertheless, this process is clearly determined by the particle size and the formation mechanisms for the shear localization.

4. CONCLUSIONS

Under large strain, high-strain rate deformation, shear localization is a favorable mechanism for granular materials. Approximately 0–18% of the global strain is accommodated in shear bands, with a characteristic shear-band spacing of 0.4–1.2 mm. The shear-band displacement, spacing between shear bands and the formation mechanisms for the shear bands are determined by the particle size.

Two different formation mechanisms for the shear bands are identified: comminution and particle rearrangement. Comminution is the dominant mechanism in the coarse granular SiC, and the mechanism is similar to the one for the fragmented SiC. During deformation, the particles are crushed and broken down, and the resultant comminuted particles can be rearranged to pack more efficiently. The shear-band displacement in this type granular SiC is negligible. Comminution is also observed in the medium granular SiC, but is never seen in the fine granular SiC. Shear bands of the medium and fine SiC granular materials can be formed through the rearrangement of the original particles. The particle comminution is determined by the particle size. Large particles contain more flaws and can be broken down easily into small pieces.

With sufficiently high shear-band displacement, the shear bands can be heated up to very high temperatures to form a thin layer of dense material. The driving force for this temperature rise is the plastic deformation of SiC, and this bonding process is significant in the medium granular SiC.

Acknowledgements—This research is supported by the U.S. Army Research Office through AASERT (DAAH04-94-G-0314) and MURI (DAAH04-96-1-0376) programs, and Institute for Mechanics and Materials (fellowship of C. J. Shih). The cylinder collapse experiments were carried out by A. A. Stertser, IHRH, Novosibirsk, Russia; his assistance is greatly appreciated. The authors wish to acknowledge the valuable help from R. C. Dickey. Discussions with Sairam Sundaram are gratefully acknowledged.

REFERENCES

1. Shockey, D., Marchand, A. H., Skaggs, S. R., Cort, G. E., Birckett, M. W. and Parker, R., *Int. J. Impact Eng.*, 1990, **9**, 263.
2. Viechnicki, D. J., Slavin, M. J. and Kliman, M. I., *Cer. Bull.*, 1991, **70**, 1035.
3. Meyers, M. A., *Dynamic Behavior of Materials*. John Wiley, New York, NY, 1994, p.597.
4. Curran, D. R., Seaman, L., Copper, T. and Shockey, D. A., *Int. J. Impact Eng.*, 1993, **13**, 53.
5. Hauver, G., Netherwood, P., Benck, R. and Kecskes, L., in *Proc. Army Symposium on Solid Mechanics*. Plymouth, MA, 1993.
6. Hauver, G., Netherwood, P., Benck, R. and Kecskes, L., Enhanced ballistic performance of ceramics. Paper presented at 19th Army Science Conf., Orlando, FL, 20–24 June 1994.
7. Rapacki, E. J., Hauver, G. E., Netherwood, P. H. and Benck, R., Ceramics for armors—A material system perspective. Paper presented at 19th Annual TARDEC Ground Vehicle Survivability Symp., Monterey, CA, 26–28 March 1996.
8. Rudnicki, J. W. and Rice, J. R., *J. Mech. Phys. Solids*, 1975, **23**, 371.
9. Vardoulakis, I., *Int. J. Num. Analyt. Mech. Geomech.*, 1980, **4**, 103.
10. Vardoulakis, I., *Int. J. Solids Struct.*, 1981, **17**, 1085.
11. Vardoulakis, I., *Acta Mechanica*, 1983, **49**, 57.
12. Vardoulakis, I. G. and Graf, B., in *Proc. IUTAM Conf. of Deformation and Failure of Granular Metals*. Delft, 1982, p. 485.
13. Scarpelli, G. and Wood, D. M., in *Proc. IUTAM Conf. of Deformation and Failure of Granular Metals*. Delft, 1982, p. 473.
14. Desrues, J., Lanier, J. and Stutz, P., *Eng. Fract. Mech.*, 1987, **21**, 909.
15. Muehlhaus, H.-B. and Vardoulakis, I., *Geotechnique*, 1987, **37**, 271.
16. Kolymbas, D. and Rombach, G., *Ingenieur-Archiv*, 1989, **59**, 177.
17. Bardet, J. P., *J. Eng. Mech.*, 1991, **117**, 1466.
18. Schaeffer, D. G., *Proc. R. Soc. Lond.*, 1992, **A436**, 217.
19. Saada, A. S., Bianchini, G. F. and Liang, L., *Geotechnique*, 1994, **44**, 35.
20. Spencer, A. J. M., *Mechanics of Solids*. Pergamon Press, Oxford, 1982.
21. Chang, C. C. and Misra, A., *Eng. Mech.*, 1989, **115A**(4), 705.
22. Klopp, R. W. and Shockey, D. A., *J. Appl. Phys.*, 1991, **70**, 7318.
23. Espinosa, H. D. and Clifton, R. J., *ASME Special Technical Publication AMD-130*, ed. K. S. Kim. ASME, Atlanta, Georgia, 1991, p. 37.
24. Espinosa, H. D., *Rev. Sci. Instr.*, 1996, **11**, 3931.
25. Nesterenko, V. F., Meyers, M. A. and Chen, H. C., *Acta mater.*, 1996, **44**, 2017.
26. Shih, C. J., Nesterenko, V. F. and Meyers, M. A., *J. Appl. Phys.*, 1998, **83**, 4660.
27. Bondar, M. P. and Nesterenko, V. F., *J. de Physique IV*, 1991, **1**, C3–163.
28. Nesterenko, V. F. and Bondar, M. P., *Dymat J.*, 1994, **1**, 245.
29. Nesterenko, V. F., Meyers, M. A., Chen, H. C. and LaSalvia, J. C., *Metall. mater. Trans. A*, 1995, **26A**, 2511.
30. Chen, H. C., Meyers, M. A. and Nesterenko, V. F., in *Shock Compression of Condensed Matter*, ed. S. C. Schmidt and W. C. Tao. AIP Press, Woodbury, New York, 1995, p. 607.
31. Nesterenko, V. F., Meyers, M. A. and Wright, T. W., in *Metallurgical and Materials Applications of Shock Wave and High-Strain-Rate Phenomena*, ed. L. K. Murr, K. P. Standhamme and M. A. Meyers. Elsevier Science, Amsterdam, 1995, p. 397.
32. Grady, D. E. and Kipp, M. E., *Int. J. Rock Mech. Min. Sci.*, 1980, **17**, 147.
33. Potapov, A. V. and Campbell, C. S., *Powder Technology*, 1997, **94**, 109.
34. Mehrabadi, M. M., Nemat-Nesser, S., Shodja, H. M. and Subhash, G., in *Micromechanics of Granular Materials*, ed. M. Satake and J. T. Jenkins. Elsevier Science, Amsterdam, 1988, p. 253.
35. Meyers, M. A. and Meyers, P. P., *Soc. of Mining Eng. of AIME*, 1984, **174**, 1875.
36. Oka, Y. and Majima, H., *Can. Metall. Quart.*, 1970, **9**, 429.
37. Krosche, E. R., A theoretical study of brittle fracture in rocks for applications in comminution. M.S. thesis, New Mexico Institute of Mining and Technology, Socorro, NM, 1985.
38. Griffith, A. A., in *Proc. 1st Int. Congress for Applied Mechanics*, ed. C. B. Biezeno and J. M. Burgers, 1924, p. 55.
39. McClintock, F. A. and Walsh, J. B., in *Proc. 4th U.S. Congress for Applied Mechanics*, Vol. 2. AISME, New York, 1962, p. 1015.
40. Weibull, W., *J. Appl. Mech.*, 1951, **9**, 293.
41. Shih, C. J. and Ezis, A., *SPIE Proceedings*, 1995, **2543**, 24.
42. Ashby, M. F. and Hallam, S. D., *Acta metall.*, 1986, **34**, 497.
43. Horii, H. and Nemat-Nasser, S., *Phil. Trans. R. Soc. Lond.*, 1986, **A319**, 337.
44. Massalski, R. W. and Abbaschian, G. J., *Binary Phase Diagram*. American Society of Metals, Metal Park, OH, 1986, p. 882.
45. Srinivasan, M., *Treatise on Materials Science and Technology*,, 1989, **29**, 99.
46. Lankford, J., *J. Am. Ceram. Soc.*, 1979, **62**, 310.
47. Sundaram, S., Pressure-shear plate impact studies of alumina ceramics and the influence of an intergranular glassy phase. Ph.D. dissertation, Brown University, Providence, RI, 1998.
48. Rudnicki, J. W. and Rice, J. R., *J. Mech. Phys. Sol.*, 1975, **23**, 371.
49. Johnson, G. R., Holmqinst, T. J., Lankford, J., Anderson, C. E. and Walker, J., A computational constitutive model and test data for ceramics subjected to large strains, high strain rates, and high pressure. Final Technical Report, DOE Contract No. DE-AC04-87AL-42550, 1990.
50. Sairam, S. and Clifton, R. J., in *Mechanical Testing of Ceramics and Ceramic Composites*, vol. 197. AMD, ASME, New York, 1994, p. 23.
51. Grady, D. E., *Mech. Matls.*, 1998, **8**, in press.
52. Adams, M. A., Jet Propulsion Lab, Pasadena, CA, private communication, 1997.
53. Miller, J., Ceradyne Inc., Costa Mesa, CA, private communication, 1997.

APPENDIX A

The stress components inside the sphere are given as follows (originally derived by Oka and Majima [36], and examined and corrected by Krosche [37]):

$$\sigma_r = \frac{2F}{\pi D^2}\left[1 + \sum_{n=1}^{\infty}\left\{\frac{\nu - 2n^2 + n + 1}{n} + \frac{2\nu + 4n^2 + 4n - 1}{2n+1}\left(\frac{a}{r}\right)^2\right\} \cdot \frac{(4n+1)(1+\cos\theta_o)P'_{2n}(\cos\theta_o)P_{2n}(\cos\theta)}{2\{(4n^2+2n+1)+(4n+1)\nu\}}\left(\frac{r}{a}\right)^{2n}\right]$$

$$\sigma_\theta = \frac{2F}{\pi D^2}\left[1 + \left\{\sum_{n=1}^{\infty}\left(\frac{1-n+(4n+1)\nu}{n} + \frac{4n^2+4n-1+2\nu}{2n(4n^2-1)}\left(\frac{a}{r}\right)^2\right)P_{2n}(\cos\theta)\right.\right.$$
$$+ \sum_{n=1}^{\infty}\left(\frac{4\nu - 2n - 5}{2n(2n+1)} + \frac{4n^2+4n-1+2\nu}{2n(4n^2-1)}\left(\frac{a}{r}\right)^2\right)(\sin^2\theta \cdot P''_{2n}(\cos\theta)$$
$$\left.\left. - \cos\theta \cdot P'_{2n}(\cos\theta))\right\} \cdot \frac{(4n+1)(1+\cos\theta_o)P'_{2n}(\cos\theta_o)}{2\{(4n^2+2n+1)+(4n+1)\nu\}}\left(\frac{r}{a}\right)^{2n}\right]$$

$$\sigma_\phi = \frac{2F}{\pi D^2}\left[1 + \left\{\sum_{n=1}^{\infty}\left(\frac{1-n+(4n+1)\nu}{n} + \frac{4n^2+4n-1+2\nu}{2n(4n^2-1)}\left(\frac{a}{r}\right)^2\right)P_{2n}(\cos\theta)\right.\right.$$
$$\left.\left. + \sum_{n=1}^{\infty}\left(\frac{5+2n-4\nu}{2n(2n+1)} - \frac{4n^2+4n-1+2\nu}{2n(4n^2-1)}\left(\frac{a}{r}\right)^2\right)\cos\theta \cdot P'_{2n}(\cos\theta)\right\} \cdot \frac{(4n+1)(1+\cos\theta_o)P'_{2n}(\cos\theta_o)}{2\{(4n^2+2n+1)+(4n+1)\nu\}}\left(\frac{r}{a}\right)^{2n}\right]$$

$$\tau_{r\theta} = \frac{2F}{\pi D^2}\left[\sum_{n=1}^{\infty}\frac{(4n+1)(4n^2+4n-1+2\nu)(1+\cos\theta_o)P'_{2n}(\cos\theta_o)P'_{2n}(\cos\theta)\cdot\sin\theta}{4n(2n+1)\{(4n^2+2n+1)+4n(4n+1)\upsilon\}} \cdot \left\{1 - \left(\frac{a}{r}\right)^2\right\}\left(\frac{r}{a}\right)^{2n}\right]$$

$$\tau_{\theta\phi} = 0$$

$$\tau_{\phi r} = 0$$

where P_{2n}, P'_{2n} and P''_{2n} are the Legendre polynomials.